Atmos. Chem. Phys. Discuss., 13, 21703–21763, 2013
www.atmos-chem-phys-discuss.net/13/21703/2013/
doi:10.5194/acpd-13-21703-2013
© Author(s) 2013. CC Attribution 3.0 License.

Atmospheric Chemistry and Physics Discussions

This discussion paper is/has been under review for the journal Atmospheric Chemistry and Physics (ACP). Please refer to the corresponding final paper in ACP if available.

Overview of a prescribed burning experiment within a boreal forest in Finland

A. Virkkula[1,2], J. Levula[1,3], T. Pohja[3], P. P. Aalto[1], P. Keronen[1], S. Schobesberger[1], C. B. Clements[4], L. Pirjola[5], A.-J. Kieloaho[1], L. Kulmala[6], H. Aaltonen[7], J. Patokoski[1], J. Pumpanen[7], J. Rinne[1], T. Ruuskanen[1], M. Pihlatie[1], H. E. Manninen[1], V. Aaltonen[2], H. Junninen[1], T. Petäjä[1], J. Backman[1], M. Dal Maso[1], T. Nieminen[1], T. Olsson[2], T. Grönholm[8], V.-M. Kerminen[1], D. M. Schultz[1,2,9], J. Kukkonen[2], M. Sofiev[2], G. de Leeuw[1,2], J. Bäck[7], P. Hari[7], and M. Kulmala[1]

[1]Department of Physics, University of Helsinki, 00014, Helsinki, Finland
[2]Finnish Meteorological Institute, Erik Palménin aukio 1, 00101, Helsinki, Finland
[3]Hyytiälä Forestry Field Station, University of Helsinki, 35500, Korkeakoski, Finland
[4]Department of Meteorology and Climate Science, San José State University, 95192, San José CA, USA
[5]Department of Technology, Metropolia University of Applied Sciences, 00079, Helsinki, Finland
[6]Finnish Forest Research Institute, P.O. Box 18, Vantaa, Finland

[7]Department of Forest Sciences, P.O. Box 27, 00014, University of Helsinki, Helsinki, Finland
[8]Finnish Environment Institute, Joensuu Office, 80101 Joensuu, Finland
[9]Centre for Atmospheric Science, School of Earth, Atmospheric and Environmental Sciences, University of Manchester, Simon Building, Oxford Road, Manchester, M13 9PL, UK

Received: 20 June 2013 – Accepted: 29 July 2013 – Published: 22 August 2013

Correspondence to: A. Virkkula (aki.virkkula@helsinki.fi)

Published by Copernicus Publications on behalf of the European Geosciences Union.

Abstract

A prescribed burning of a boreal forest was conducted on 26 June 2009 in Hyytiälä, Finland, to study aerosol and trace gas emissions from wildfires and the effects of fire on soil properties in a controlled environment. A 0.8 ha forest near the SMEAR II was cut clear; some tree trunks, all tree tops and branches were left on the ground and burned. The amount of burned organic material was ~ 46.8 t (i.e., ~ 60 t ha^{-1}). The flaming phase lasted 2 h 15 min, the smoldering phase 3 h. Measurements were conducted on the ground with both fixed and mobile instrumentation, and from a research aircraft. In the middle of the burning area, CO_2 concentration peaks were around 2000–3000 ppm above the baseline and peak vertical flow velocities were 6 ± 3 m s^{-1}, as measured a 10-Hz 3-D sonic anemometer placed within the burn area. Peak particle number concentrations were approximately $1–2 \times 10^6$ cm^{-3} in the plume at a distance of 100–200 m from the burn area. The geometric mean diameter of the mode with the highest concentration was at 80 ± 1 nm during the flaming phase and in the middle of the smoldering phase but at the end of the smoldering phase the largest mode was at 122 nm. In the volume size distributions geometric mean diameter of the largest volume mode was at 153 nm during the flaming phase and at 300 nm during the smoldering phase. The lowest single-scattering albedo of the ground-level measurents was 0.7 in the flaming-phase plume and ~ 0.9 in the smoldering phase. The radiative forcing efficiency was negative above dark surfaces, in other words, the particles cool the atmosphere. Elevated concentrations of several VOCs (including acetonitrile which is a biomass burning marker) were observed in the smoke plume at ground level. The forest floor (i.e., richly organic layer of soil and debris, characteristic of forested land) measurements showed that VOC fluxes were generally low and consisted mainly of monoterpenes, but a clear peak of VOC flux was observed after the burning. After one year, the fluxes were nearly stabilised close to the level before the burning. The clearcutting and burning of slash increased the total long-term CO_2 release from the soil, altered the soil's physical, chemical and biological properties such as increased the available nitrogen contents of the soil, which in turn, affected the level of the long-term fluxes of greenhouse gases.

1 Introduction

Gaseous and aerosol emissions from wildfires have significant climatic and health effects ranging from local to hemispheric scales (e.g., Andreae, 1991; Penner et al., 1992; Grell et al., 2011). In the Northern Hemisphere, smoke from wildfires can be transported over long distances from the boreal forest areas in Eurasia and North America to the Arctic (e.g., Radke et al., 1991; Goldammer et al., 1996; Lavoué et al., 2000; Randerson et al., 2006; Law and Stohl, 2007; Shindell et al., 2008; Paris et al., 2009; Lamarque et al., 2010; AMAP, 2011). Smoke originated from wildland fires in Eastern Europe has also been shown to affect extensive regions in Western and Central Europe (Klein et al., 2012; Saarnio et al., 2010). Wildfire emissions have both warming and cooling effects on climate. The greenhouse gases and black carbon emitted in burning heat the atmosphere but aerosols may also have a cooling effect, depending on their optical and cloud-forming properties. Surface albedo changes due to fires have also a significant climatic effect. For instance, Randerson et al. (2006) showed that the warming impact of increasing boreal forest fires may be limited or even result in regional cooling because of loss of canopy overstory and consequently higher albedo values during winter and spring.

Ongoing wildfires and burned areas can be observed from space by using satellite imagery (e.g., Flannigan and Haar, 1986; Lentile et al., 2006; French et al., 2008; Sofiev et al., 2009; van der Werf et al., 2010). Satellite images give information on the area and amount that is burning and also on the amount of smoke released. However, they do not give direct information on the composition of smoke. To estimate the amount of aerosols and trace gases emitted, emission factors, defined as the amount of emitted aerosol or trace gases per mass unit of burned biomass, are needed. Recent reviews of emission factors include Andreae and Merlet (2001), Reid et al. (2005a, b), Janhäll

et al. (2010), Akagi et al. (2011), Simpson et al. (2011), and Yokelson et al. (2013). van der Werf et al. (2010) estimated the total global carbon emissions due to deforestation, savanna, forest, agricultural, and peat fires by using a biogeochemical model and satellite-derived estimates. They estimated that the boreal region accounted for about 9 % of total global carbon emissions from fires.

Detailed measurements of gas and aerosol emissions are difficult in real wildfires: the fire may be too large and uncontrolled and at a difficult location for taking instruments even near to it. For this purpose a prescribed burning of forest is more suitable. The controlled burning of the forest is used for the fire prevention, site preparation and maintaining habitat quality (Bowman et al., 2009). The total area of wildlife prescribed burns in the USA was nearly 1 million hectares during 2011 (National Interagency Fire Center, 2011). In Finland, there is a long tradition of burning forests. The use of burn-beating cultivation to produce corn and root crops existed for several hundred years and ended around 1910 (Heikinheimo, 1915). In the 1920s, prescribed burning of clear-cut areas was begun (Viro, 1969). The idea of prescribed burning is to burn the logging waste, surface vegetation and the uppermost part of the raw humus layer. This practise promotes the regeneration of the tree stand and is normally followed by the seeding of Scots Pine and occasionally Silver Birch. Prescribed burning was widely used in Finland in the 1950s and 1960s, with over 10 000 ha typically burned annually. Since then, more effective mechanical soil-preparation methods superseded prescribed burning (Finnish Forest Research Institute, 1992). One reason for the reduction in the areas burned was also the fear of the fire getting out of control. Nowadays, 500–1000 ha are burned each year (Finnish Forest Research Institute, 2012), and the main reason for the burnings is to enhance biodiversity.

The use and effects of controlled burning of forest is investigated in University of Helsinki. As part of this work, we conducted a controlled prescribed burning of forest about 300–500 m south-southwest from the SMEAR II measurement station (Station for Measuring Ecosystem–Atmosphere Relations) in Hyytiälä, Finland (61°50′47″ N, 24°17′42″ E, 181 m a.m.s.l.) (Hari and Kulmala, 2005) on 26 June 2009. The experiment was an integral part of two large projects: the European Integrated project on Aerosol Cloud Climate and Air Quality Interactions (EUCAARI) (Kulmala et al., 2011) and An Integrated Monitoring and Modelling System for Wildland Fires (IS4FIRES) (Saarikoski et al., 2007; Sofiev et al., 2009).

A 0.8 ha forest area near SMEAR II was cut clear. Some tree trunks, all tree tops and all branches were left on the ground and burned. During burning, we conducted measurements on the ground, with both fixed and mobile instrumentation, and from a research aircraft. Ground-based instrumentation included the SMEAR II station and meteorological and ecological measurements on and around the site. We measured ground-level dispersion of particles and trace gases both by using the research van *Sniffer* and by walking in the forest with portable particle counters at different distances from the burning area. We measured the vertical and horizontal dispersion of the plume with instruments installed in a Cessna 172. Soil temperature, humidity, and trace gas efflux were measured within the burn and unburned reference areas.

The general goal of the experiment was to collect data for estimating the effect of natural forest fires on air quality and climate. More detailed goals were (1) to obtain emission factors of aerosols and gases, (2) characterization of the climatically relevant physical properties of the smoke aerosol, such as size and optical properties, (3) to quantify the connections between ground-based smoke observations and satellite remote sensing, (4) obtain data for testing an improving modeling of atmospheric dispersion of the fire plume, (5) to study the recovery of the forest after burning, and (6) to quantify the changes taking place in soil carbon stocks and greenhouse gas (CO_2, CH_4 and N_2O) fluxes following clear-cutting and prescribed burning.

The purpose of this article is to provide an overview of the experiment by describing the preparations for the experiment, the estimates of burned biomass, meteorological conditions during the experiment, characterization of the aerosols and gases emitted, and the observed dispersion of aerosols both on ground level and in the airborne measurements. The aim is also to analyze the performance of the used setup for making studies on wildfires.

2 Methods

2.1 The site preparation

A suitable burn area was found in summer 2008 approximately 300–500 m south-southwest of the measurement buildings of the SMEAR II station. We selected the site to be burned so that prevailing southwesterly wind would bring the smoke aerosols and gases to the SMEAR II station during the burning, specifically, a wind direction from 180–200°. To determine the suitability of the burn area, the 30 min averaged wind direction from the SMEAR II mast data over the layer 33.6 m to 73 m was averaged from all Junes 1996–2008 to get the mean wind direction above the tree-tops. Based on this climatology, wind directions of 180–200° occur 9.6 % of the time with no particular preference for a specific time of day. When the wind occurs in this direction, the wind is frequently 3 m s^{-1}, which is less than the 5 m s^{-1} required for a safe burn.

In addition to the burn area, we also selected a control site near the burning area (Fig. 1). At the burn site, there was a mature spruce-dominated stand with the stem volume per hectare of about 400 m^3. The area was cut clear in February 2009. After the clearcut most tree trunks were transported away; some of them and all tree tops and all branches were left on the ground in the burn area. An estimation of the biomass was done before and after the burning.

2.2 Estimation of burned organic material

The tree stand was measured in July 2008 from 13 relascope plots from which the species, diameter at breast height (DBH), diameter at the height of 6.0 m, the living crown length and height (*H*) were recorded for each tree. Then, biomass models (Repola et al., 2007) were used to calculate the biomass for the different tree components. The merchantable wood was harvested in February 2009, after which all the non-merchantable trees were also felled. After burning the amount of unburned wood was sampled from 21 plots of 0.5 m^2. All the wood was collected from the plots, dried

(24 h, 105 °C) and weighted. The amount of burned tree biomass was finally calculated as an extraction of the non-merchantable tree biomass (tree tops, branches and non-merchantable trees) and unburned wood biomass. The surface vegetation, dominated by feather mosses and dwarf shrubs, was systematically sampled from 13 plots of 0.0625 m^2 in July–August. The vegetation was cut along the surface of the litter layer, collected, dried (24 h, 105 °C) and weighed. The organic matter content of the uppermost, organic soil layers (litter layer and humus layer) was systematically sampled both before the clearcut in August 2008 and soon after the burning in July 2009. A total of 25 samples were collected on both occasions with a 45 mm-diameter soil auger. The samples were dried (24 h, 105 °C) and weighed. The mass of burned organic material in the organic soil layer was calculated as an extraction of the mass before and after the burning.

2.3 Gas, aerosol and meteorological measurements

A list of the measurements conducted during the campaign is presented in Table 2. In short, trace gas concentrations, aerosol physical properties, aerosol chemical composition, and meteorological parameters were measured both at fixed sites and on mobile platforms.

2.3.1 Measurements at fixed positions

At the SMEAR II measurement station both aerosols and gases were measured with the setup described by Hari and Kulmala (2005). Measurements were conducted at five different locations: the main building of the station, the 73-m-high SMEAR II mast, the aerosol cottage, the Relaxed Eddy Accumulation (REA) cottage, and the Aerosol Optical Depth Tower (AODTWR) about 100 m east of the aerosol cottage. The above measurements are within 300–400 m of the burn area (Fig. 1b).

The concentrations of CO_2, H_2O, O_3, NO, NO_x, SO_2 and CO were measured continuously at six heights along the 73 m mast. The instruments were located in the

main building and sample air was taken through six sample lines: PTFE Teflon™ tubes, each 100 m long, and 14 or 16 mm in diameter. There was a continuous flow rate of 45 L min^{-1} in the lines, which resulted in an estimated lag time of 20 s. For each gas component, there was one analyser (a dual channel instrument for NO and NO_x) for measuring the concentrations. The response times of the analysers were about 30 s, so, when sampling a new height, a flush time of about 30 s was needed. This set the signal recording time step to 1 min and the overall time spacing of the data to 6 min.

Volatile organic compounds (VOCs) were measured with Ionicon Analytik Proton Transfer Reaction Mass Spectrometers (PTR-MS, e.g., Hewitt et al., 2003) at two locations: one at the SMEAR II main building with an inlet above the roof at about 10 m a.g.l. and the other in the REA cottage with the inlet above canopy at the REA tower. The PTR-MS instrument measures charged VOCs at given mass that were assigned to the VOCs that likely dominated each signal. The assignment of mass-to-charge ratios ($= m/z$) to VOCs and the measurement setup is described by Taipale et al. (2008). Usually, m/z 69 is assigned to the biogenic VOCs isoprene and MBO, but, in this case, m/z 69 was assigned to furan, which is associated with burning processes (de Gouw and Warneke, 2006). The VOC measurements were sampled every 1 min.

An Aerodyne Aerosol Mass Spectrometer (AMS) (e.g., Jayne et al., 2000; Jimenez et al., 2003; Drewnick et al., 2005) was used for measuring the concentrations of ammonium (NH_4^+), sulfate (SO_4^{2-}), nitrate (NO_3^-), chloride (Cl^-), and organics in particles with $D_p < 600$ nm. The AMS was located in the SMEAR II main building and it took its sample from the same inlet as the PTR-MS, above the roof at about 10 m a.g.l. The AMS measurements were taken every 5 min.

In the aerosol cottage, particle number size distributions for particles of 3–1000 nm in diameter were measured with a custom-made Twin-DMPS (TDMPS) system (Aalto et al., 2001) and a TSI aerodynamic particle sizer (APS) in the aerodynamic diameter size range 0.53–20 µm. In the overlapping range of the TDMPS and the APS, the number concentrations from the TDMPS were used up to 700 nm. Data were collected every 10 min. A Neutral cluster and Air Ion Spectrometer (NAIS) was used to measure

the mobility and size distributions of atmospheric ions and neutral clusters in the size range 0.8–47 nm (e.g., Manninen et al., 2009; Asmi et al., 2009) for the first time in a wildfire smoke plume. The NAIS measurements were taken every 2 min.

The aerosol optical measurements at SMEAR II were described in detail by Virkkula et al. (2011). In short, total scattering coefficients (σ_{sp}) and backscattering coefficients (σ_{bsp}) were measured with a TSI 3λ nephelometer, averaged over a 5 min period. A Magee Scientific 7λ Aethalometer (AE-31) was used for measuring light absorption, also at a 5 min averaging time. Absorption coefficient (σ_{ap}) was calculated from the aethalometer and nephelometer data using the algorithm by Arnott et al. (2005).

Aerosol optical depth was measured with a Cimel CE-318 sunphotometer in a tower about 100 m east of the aerosol cottage (Fig. 1), above the canopy level. The sunphotometer made one instantaneous measurement every 15 min. In the same tower, light absorption coefficient at a wavelength (λ) of 637 nm was measured with a Multi-Angle Absorption Photometer (MAAP). The MAAP reports the absorption coefficient as black carbon concentrations using the mass absorption coefficient of 6.6 m^2 g^{-1}. MAAP measurements were available every 1 min.

In addition to the SMEAR II measurements, we installed meteorological sensors on top of poles within and around the area to be burned. The poles were prepared by cutting the branches of five trees that were left standing in the slash. Four poles were outside the burning area, and one was within it (Fig. 1a). The distances of the poles 1, 2, 3, and 4 from the perimeter of the burn area were 10, 8, 9 and 6 m, respectively. In situ meteorological sensors (Vaisala WTX510) were deployed on the burn perimeter, and a sonic anemometer (ATI Sx-Probe) and Vaisala GMP-343 CO_2 sensor were placed within the burn area on the top of a pole at about 12 m in height. Total heat flux was measured at the surface with a water-cooled Hukseflux, Inc. SBG01 sensor.

2.3.2 Mobile measurements

Ground-level dispersion of aerosols and gases was measured in *Sniffer*, from the Metropolia University of Applied Sciences, Helsinki, (Pirjola et al., 2004, 2006). *Sniffer*

was driven in the surrounding forest roads and stopped at several locations for some minutes. Sampling occurred above the windshield of the van at 2.4 m altitude. Particle number concentration and size distribution were measured by an Electrical Low Pressure Impactor (ELPI, Dekati Ltd) at a flow rate of 10 L min^{-1} (Keskinen et al., 1992). ELPI was equipped with a filter stage (Marjamäki et al., 2002) and a stage to enhance the particle size resolution for nanoparticles (Yli-Ojanperä et al., 2010). The ELPI classifies particles in the size range of 7 nm–10 µm (aerodynamic diameter) to 12 classes with samples every 1 s. *Sniffer* also monitored concentrations of CO, NO, NO_2 and CO_2 at one-second intervals. Furthermore, $PM_{2.5}$ and PM_{10} were recorded by two TSI DustTrak aerosol monitors. A weather station on the roof of *Sniffer* at 2.9 m height provided meteorological parameters (temperature, relative humidity, wind speed and wind direction). A global positioning system (GPS) was used to record the van's speed and the driving route.

In addition to *Sniffer*, the dispersion on the ground level was measured by students walking around the area with three portable TSI model 3007 condensation particle counters (CPCs) and GPS receivers. There were three different routes at three distances from the burning area. The CPCs used in the nearest two routes were equipped with diluters because, according to the manual, the model 3007 CPC measures concentrations up to 10^5 cm^{-3}. The diluters were calibrated afterwards and a flow rate of 0.7 L min^{-1} in the 3007 CPC produced a dilution ratio of about 0.32. Thus, the concentrations from the two nearest routes were divided by 0.32, resulting in the upper limit of the concentration range increasing to about 3×10^5 cm^{-3}.

Vertical and horizontal dispersion were measured with instruments installed in a Cessna 172, (Schobesberger et al., 2013). There were three CPCs for measuring particle number concentrations at three cutoffs (3, 6, and 10 nm). The 3 nm cutoff was with a TSI model 3776 CPC. The other two were TSI model 3772 CPCs equipped with 1 : 10 diluters and set up for cutoff sizes 6 nm and 10 nm. In the present article, the discussion of particle number concentrations is based on the model 3776 CPC only. Scattering coefficient (σ_{sp}) at λ = 545 nm was measured with a Radiance Re-

search model 903 nephelometer, and absorption coefficient (σ_{ap}) was measured with a Radiance Research 3-λ Particle Soot Absorption Photometer (PSAP) at λ = 467 nm, 530 nm, and 660 nm. A LICOR LI-84 measured CO_2 concentrations. The data were saved at 1-Hz frequency. The scattering and absorption coefficients will be discussed in the companion paper elsewhere.

2.3.3 Soil and flux measurements

The changes in soil physical, chemical and biological environment were monitored with a long-term perspective, as similar high frequency instrumentation described above for atmospheric aerosol and trace gas concentrations, are not available for the soil parameters. Also, although the soil conditions do change rapidly during and after the fire, many of the biological processes and responses to changing conditions have a lack-time, requiring several years of monitoring. These slowly changing responses were expected for instance in soil pH and the concentrations of available nitrogen, as well as soil greenhouse gas fluxes.

Long-term ecological measurements were begun in the mature forest in 2008 before the clear cut and partial burning. The measurements were performed at three sites: (1) on the area that was later clear cut, (2) on the area that was later clear cut and also burned and (3) on an area that remained as a mature forest. These measurements comprised automatic soil temperature and moisture measurements in the organic layer and in the A and B mineral soil horizons, manual measurements of the heights of soil organic layers, and the total carbon and nitrogen content, as well as available nitrogen species and pH in organic and mineral soil horizons. The soil horizon is a layer parallel to the soil surface, whose physical characteristics differ from the layers above and beneath. The measurement campaign ended in late 2011, two and half years after the burning

The long-term effects of the burning of slash on the CO_2 and CH_4 fluxes from the soil were quantified by manual chamber measurements from the burned area every two weeks together with the corresponding measurements from the clear cut and a control

forest (Kulmala et al., 2012, 2013). The flux measurements were performed by placing a chamber on a collar inserted approximately 5 cm within the soil. Eleven collars were inserted for CO_2 measurement and 8 collars were inserted for CH_4 measurement, respectively, at each site, and one closure took 4 min for CO_2 and 35 min for CH_4, as described in detail by Kulmala et al. (2013) and Pihlatie et al. (2013). During 2008–2010, CO_2 fluxes at each site were also measured using an automatic chamber described in detail by Kulmala et al. (2010, 2011). We approximated the cumulative release of CO_2 after the treatments by interpolating the average effluxes from each treatment separately.

The emission of forest-floor VOCs were measured five times at the burn site during 2008–2010. The VOC fluxes were measured on five permanently installed collars with a manual steady-state chamber system. The VOC sampling and analysis method is described by Aaltonen et al. (2011).

2.4 Formulas used for data processing

By using the measurements in the 12 m pole within the burning area, the turbulent sensible heat flux was calculated from the covariance of the vertical velocity and sonic temperature perturbation as

$$H_s = \rho C_p \overline{w' T'} \tag{1}$$

where ρ is the air density, assumed to be constant, and C_p is the heat capacity of air at constant pressure. The turbulent kinetic energy (TKE) is the sum of the velocity variances:

$$\mathrm{TKE} = \frac{1}{2}\left(\sigma_u^2 + \sigma_v^2 + \sigma_w^2\right) \tag{2}$$

In the smoke plume concentrations of trace gases and aerosols were elevated. The concentration of trace gas X above the background is defined as the excess concentration and denoted as ΔX. The excess concentrations of CO (= ΔCO) and CO_2

(= ΔCO_2) can be used for estimating the burning efficiency. The modified combustion (MCE) efficiency is defined as

$$\mathrm{MCE} = \frac{\Delta CO_2}{\Delta CO_2 + \Delta CO}. \tag{3}$$

MCE is often used as an indicator of whether the combustion is flaming or smoldering (e.g., Ward and Hao, 1992; Yokelson et al., 1996; Hobbs et al., 2003; van Leeuwen and van der Werf, 2011).

The aerosol number size distributions were used for calculating volume size distributions and the integrated mass concentrations were calculated by assuming a density of 1.5 g cm^{-3}. Three to five lognormal modes were fitted to the data up to 10 µm. The fitting yields the modal parameters (geometric mean diameter (D_g), geometric standard deviation (σ_g), and number or volume concentration of the mode).

The in situ aerosol optical data were analyzed as discussed in Virkkula et al. (2011). Here we calculated three intensive aerosol optical properties: the single-scattering albedo (ω_0), the Ångström exponent of scattering (α_{sp}), and the backscatter fraction (b).

$$\omega_0 = \frac{\sigma_{sp}}{\sigma_{sp} + \sigma_{ap}} \tag{4}$$

is a measure of the darkness of aerosols: for purely scattering aerosols it equals 1 and for black carbon (BC) approximately 0.3 ± 0.1. The Ångström exponent of scattering α_{sp} describes the wavelength dependency of scattering and we calculated it for the nephelometer wavelength range by taking logarithm of scattering coefficients and the respective wavelengths and fitting the data line to the line

$$\ln(\sigma_{sp}) = -\alpha_{sp} \ln(\lambda) + C \tag{5}$$

where C is a constant not relevant in this work. In general large values ($\alpha_{sp} > 2$) indicate the dominance of small particles and small values ($\alpha_{sp} < 1$) the dominance of large

particles. This relationship is not unambiguous, however (e.g., Schuster et al., 2006; Virkkula et al., 2011).

The backscatter fraction b

$$b = \frac{\sigma_{bsp}}{\sigma_{sp}} \tag{6}$$

where σ_{bsp} is the backscattering coefficient, is a measure related to the angular distribution of light scattered by aerosol particles. From b it is possible to estimate the average upscatter fraction β and aerosol asymmetry parameter which are key properties controlling the aerosol direct radiative forcing (e.g., Andrews et al., 2006). In general, larger particles scatter less light backwards than small particles so the size relationship of b is qualitatively similar to that of α_{sp}.

The radiative forcing efficiency (dF/δ), i.e., aerosol forcing per unit optical depth (δ) was calculated from:

$$\frac{\Delta F}{\delta} = -DS_0 T_{at}^2 (1 - A_c)\, \omega_0 \beta \left\{ (1 - R_s)^2 - \left(\frac{2R_s}{\beta} \right) \left[\left(\frac{1}{\omega_0} \right) - 1 \right] \right\} \tag{7}$$

where D is the fractional day length, S_0 is the solar constant, T_{at} is the atmospheric transmission, A_c is the fractional cloud amount, R_s is the surface reflectance, and β is the average upscatter fraction calculated from b. If the non-aerosol-related factors are kept constant and if it is assumed that β has no zenith angle dependence this formula can be used for assessing the intrinsic radiative forcing efficiency by aerosols (e.g., Sheridan and Ogren, 1999; Delene and Ogren, 2002). The constants used were D = 0.5, S_0 = 1370 W m^{-2}, T_{at} = 0.76, A_c = 0.6, and R_s = 0.15 as suggested by Haywood and Shine (1995) and β was calculated from $\beta = 0.817 + 1.8495b - 2.9682b^2$ (Delene and Ogren, 2002). For R_s also the value of 0.85 was used to assess the effect of the aerosols above snow surfaces.

3 Results and discussion

3.1 General description of the burning

The measurement setup was ready at the beginning of May 2009, waiting for the wind to blow from the right direction (175–215°) during dry conditions. In the morning of 26 June wind was blowing from this direction and the sky was clear. A handheld smoke signal was ignited soon after 07:00 East European Time (EET = UTC +2 h) in order to make the final decision of when to start the fire. The conditions were acceptable, so the area was set on fire at 07:45 EET. (All times presented below will be in EET, not in East European Summer Time.) The burning was performed against the wind as a broadcast burn; first the fire was ignited under the wind and then ignition slowly proceeded in both directions (Fig. 1a). The idea was to slowly burn the edges of the site until a horseshoe-like shape was achieved and more than half of the area was burned. This phase of our experiment took about 110 min. Then, the edges were rapidly ignited in both directions over the wind so that the edges of the site were shut with the fire. Thereafter, the fire proceeded rapidly downwind, and flaming was over within about 25 min. The flaming or active burning was over at 10:00 EET, and there was only a little visible smoke at 13:00 EET. These times will be shown in the figures below as the indicators of the flaming and smoldering phases of the burning, although the ends of both periods were not well defined. There were flames in some parts of the area while most of it was already smoldering, and smoldering biomass does not always emit visible smoke. For the purposes of this paper, we define the *plume* as approximately the visible column of smoke and the *fire front* as the leading edge of the flames.

After the burning the amount of burned organic material was estimated as described above (Sect. 2.2). The amount of unburned wood was 30 700 kg. The burned area was approximately 0.81 ha so the amount of burned wood biomass was about 38 030 kg ha^{-1}. All the surface vegetation 1850 kg (2300 kg ha^{-1}) was burned. The mass of burned organic material in the organic soil layer was 14 200 kg (17 600 kg ha^{-1}). The total amount of burned organic material (46 800 kg,

58 000 kg ha^{-1}) was calculated as a sum of burned tree biomass, surface vegetation and organic soil layer (Table 1). Schlesinger (1991) noted that the carbon content of biomass is generally between 45 % and 50 % (by oven-dry mass). Table 1 also presents an estimated amount of carbon released by multiplying the biomass by 0.5.

3.2 Winds

Most of the smoke ascended almost vertically, as seen from the aerial photographs taken during the flaming phase of the experiment (Fig. 1) indicating that wind speed was not high and no strong temperature inversion was present to inhibit the rising smoke. That the wind speed was low is also shown by measurements in the SMEAR II 73 m mast. At the ignition time, wind speed was $< 2\,m\,s^{-1}$ at all altitudes of the tower but it increased to 2–4 m s^{-1} during the morning (Fig. 2a). After ignition, the wind direction turned from southwesterly to southeasterly. On average, the directional shear between the 8.4 m and 73 m levels was small: the average wind direction was 138° and 134° at the 8.4 m level and 140° and 136° at the 73 m level during the flaming and smoldering phases, respectively. The average (± standard deviation) wind speed was $0.55 \pm 0.26\,m\,s^{-1}$ and $0.74 \pm 0.38\,m\,s^{-1}$ at the 8.4 m level and $2.2 \pm 1.1\,m\,s^{-1}$ and $3.0 \pm 1.3\,m\,s^{-1}$ at the 73 m level during the flaming and smoldering phases, respectively.

Measurements from the sonic anemometer at the top of the 12 m pole within the burning area (Fig. 3) show that both the wind direction and wind speed varied considerably more than at the SMEAR II mast. This is explainable both by the forest around the high mast and by fire-induced winds within the open burning area. During the flaming period, the average wind direction and speed at the top of the pole were 189° and $2.5 \pm 1.1\,m\,s^{-1}$ (Fig. 3f and g) so the wind speed was slightly higher than at the top of the 73 m mast during the flaming period. The increased variability in wind speed and direction is caused by fire–atmosphere interactions that occur near the fire front and within the near-surface plume (Clements et al., 2008). An increase in wind speed has been observed to occur at the fire front or during fire-front passage during both wind-

driven grass fires (Clements et al., 2007) and crown fires (Coen et al., 1999). Maximum updraft vertical velocities and maximum temperatures indicate the location of fire front (Clements et al., 2007).

Although the small-scale features of the fire front and variability in its intensity cannot be resolved by the vertical velocity and plume temperature (Fig. 3d and e), the crude, near-surface properties of the atmosphere surrounding the combustion zone can be quantified. The fire front advanced from the northeast and northwest corners, south and around to the southern edge of the clearcut area. The fire burned as a head fire from the north to the south and through the center of the burn area. The fire was close to the mast several times, which is indicated by sharp increases in CO_2 concentration, positive vertical velocity (w) and temperature (T) (Fig. 3a, d and e). In addition, an abrupt change in wind direction also occurred during the fire-front passage (Fig. 3g). These observations of weak ambient winds, an upright plume, and higher fire intensity are consistent with plume-dominated fires (Sullivan, 2007).

The first fire-front passage occurred at 08:02–08:11 EET, T and w reached 59 °C and 5.4 m s^{-1} and the wind direction varied. The duration of the second plume passage was shorter (08:23–08:26 EET), followed by temperature increasing to a maximum of 84 °C and w increasing to 4.1 m s^{-1}. The most pronounced fire-front passage occurred at 08:35–08:52 EET when T and w reached maximum values of 148 °C and 9.0 m s^{-1}, the heat flux was in the range 20–40 kW m^{-2} (Fig. 3b), and the CO_2 concentrations were in the range 2000–3000 ppm (Fig. 3a). This period is when the fire front passed under the instruments as indicated by the sharp increase in total heat flux (Fig. 3b). However, because there was no continuous video surveillance, it cannot be excluded that the above variations were from plume impinging on tower rather than fire underneath. After 09:02 EET, the area around the mast was burning more steadily but with a decreasing intensity. At 09:03 EET, T and w maxima were 41 °C and 4.2 m s^{-1}, respectively, and at 09:36 EET, T and w maxima were 26 °C and 2.5 m s^{-1}, respectively.

Both the sensible heat flux and TKE were calculated using 10-Hz data from the sonic anemometer and averaged to 1 min in order to isolate fluxes and associated with the

fire-front passage. During the fire-front passage, the sensible heat flux increased to 20 kW m^{-2} and peaked to ~ 58 kW m^{-2} (Fig. 3b). Sharp increases in H_s indicate when the plume impinges on the mast and instrumentation, and sharp decreases in sensible heat flux indicate when the plume has passed and represent ambient conditions. The turbulent kinetic energy increased from approximately 1 m^2 s^{-2} before the plume and fire-front passage to nearly 15 m^2 s^{-2} during the fire-front passage (Fig. 3c).

In addition to the pole in the middle of the burn area, four surface meteorological stations were deployed around the outside of the burn area (Fig. 1a). Although these surface stations did not experience the fire front directly as they were situated 6–10 m outside the burn area, they sampled the plume and the ambient meteorology surrounding the burn unit. The largest changes in meteorological measurements associated with the plume were collected by sensors 3 (southwest of the burn area) and 4 (southeast of the burn area). These two sensors recorded the more intense passage of the plume (13 °C and 18 °C rises in temperature associated with the plume passage, respectively; Fig. 4a and b) than sensors 1 and 2 (4 °C and 2 °C rises; not shown). The fire came closest to sensor 3 at about 09:10 EET and sampled the plume about 09:27–09:50 EET (Fig. 4a). The fire came closest to sensor 4 at about 09:15 EET and sampled the plume about 09:25–09:35 EET (Fig. 4b).

At sensor 3 around 09:27 EET, the wind shifted from southeasterly to southerly with a weakening wind of 1.5–2 m s^{-1} (Fig. 4c). This shift was coincident with the beginning of a rise in temperature from 23 °C during which the wind shifted direction from southeasterly to southerly (Fig. 4a and c). By the time of the temperature peak of 35.8 °C at 09:35 EET, the relative humidity reached its minimum of 16.7 % with a slow drop over about the next 15 min (Fig. 4a).

In comparison, at sensor 4 around 09:21–09:24 EET, the wind shifted around to east and northeast, suggesting that this is the inflow to the fire, and decreased (less than 1 m s^{-1}, as low as 0.5 m s^{-1}) (Fig. 4d). A slow rise in temperature to 25 °C followed (Fig. 4b), when the wind reached its most westerly (241°) and increased to as much as 4.9 m s^{-1} (Fig. 4d). Despite the rise in temperature, the relative humidity peaked at

52 % at the time of the most westerly wind (Fig. 4b and d) and the mixing ratio remained elevated (peaking at over 10 g kg^{-1} above an ambient value of 7–8 g kg^{-1} when the plume was sampled). Interestingly, this sensor was the only one to record such a strong rise in relative humidity, perhaps because the sensor sampled the plume only about 10 min after its closest approach to the flames. Enhanced moisture in smoke plumes due to combustion of wildland fuels has been suggested to possibly modify plume dynamics (Potter, 2005). Direct measurements of increased plume moisture have been made previously in grass fuels (Clements et al., 2006; Kiefer et al., 2012) with increase in water vapor mixing ratio of 1–3 g kg^{-1}, and during smoldering fires in the longleaf-pine ecosystems in the southeastern United States (Achtemeier, 2006). During 09:25–09:27 EET, the temperature rose to its peak (41.1 °C), and the RH decreased from 25–30 % to 16 % at the peak temperature (Fig. 4b).

3.3 Trace gases observations at the SMEAR II mast

The trace gases O_3, NO_x, SO_2, CO and CO_2, which are routinely measured at six different altitudes in the mast, should all have clearly elevated concentrations in a biomass burning plume (e.g., Radke et al., 1991). However, in the data from the mast, the concentrations of most of them deviated very little from the background concentrations during the whole experiment (Fig. 2). The time series of trace gas concentrations measured from the mast shows that the smoke plume arriving at the mast was narrow and patchy. The clearest concentration variations were for CO (Fig. 2e). During the flaming phase, the highest CO concentration of 236 ppb was measured at 09:14 EET at an altitude of 33.6 m. This concentration was 127 ppb above the then-background value of 109 ppb, which was calculated as the running first percentile of the one-minute averages during the 30 min before and after each measurement. CO reached the peak value of 372 ppb, with the excess concentration ΔCO = 263 ppb during the smoldering phase at 12:40 EET. The last two clear CO peaks were observed at 13:37 EET when ΔCO was 246 ppb and at 14:37 EET when ΔCO was 136 ppb.

In complete combustion of hydrocarbon fuels in air, the reaction products include CO_2, water, and heat, in different proportions, and, in stoichiometric calculations, nitrogen is also considered a reaction product (e.g., Flagan and Seinfeld, 1988). If, however, the burning process is incomplete, numerous other products are formed. The important products in the gas phase are CO and several condensable organic vapours. At the high mast, the variations in CO_2 concentrations were very small (Fig. 2f), suggesting that the smoke plume did not hit the mast. There was only one 1 min data point when it increased clearly above the baseline: at 08.47 EET, the CO_2 concentration peaked at 418 ppm. The then-running CO_2 baseline was 402 ppm, calculated as for CO above, so ΔCO_2 was 16 ppm. This peak occurred at the same time as a CO peak with $\Delta CO = 62$ ppb.

A scatterplot of ΔCO_2 vs. ΔCO further confirms that their correlation was negligible (Fig. 5a). The linear regression lines for ΔCO_2 vs. ΔCO were calculated for the data where $\Delta CO > 40$ ppb to examine whether even in the clearest plumes there was a positive relationship. There was a weak positive relationship. These regression lines were used for estimating the emission ratio $\Delta CO/\Delta CO_2$. For instance during the flaming phase, $\Delta CO_2 = 0.012 \times \Delta CO + 2.4$ ppm, so when $\Delta CO = 100$ ppb, $\Delta CO_2 = 3.6$ ppm and the ratio $\Delta CO/\Delta CO_2 = 2.8\,\%$. During the smoldering phase, the regression in Fig. 4 would yield $\Delta CO/\Delta CO_2 = 6.5\,\%$ at $\Delta CO = 100$ ppb. These ratios are consistent with some published values. For instance, Andreae and Merlet (2001) presented the emission factors of several trace gases from various types of biomass burning. For extratropical forests, they give the emission factors for CO_2 of 1569 ± 131 g kg^{-1} and for CO of 107 ± 37 g kg^{-1} of burned dry biomass. From these numbers, the ratio $\Delta CO/\Delta CO_2 = 6.8\,\%$ can be calculated at the mid value and the range from 4 % to 10 % by using the uncertainties.

Yokelson et al. (1996) found that in pure flaming combustion MCE is close to 0.99 and in smoldering combustion about 0.8. Hobbs et al. (2003) deduced from those numbers that an MCE greater than 0.9 roughly indicates more than 50 % of flaming combustion and MCE greater than 0.9 more than 50 % of smoldering combustion. During the

flaming phase of the experiment, none of the MCEs were less than 0.9, but, during the smoldering phase, some of the MCE values were less than 0.9 and some were greater than 0.9 (Fig. 5b), roughly consistent with the previous results.

NO_x and SO_2, on the other hand, did have some peak concentrations above their baselines that correlated positively with ΔCO during the flaming phase (Fig. 5c and d). The NO_x concentrations had peaks in times when no other indications of the smoke plume were present – for instance the three highest peaks during the smoldering phase. A probable explanation for these peaks is car traffic around the station occurring during the burning.

The wind directions at the highest and lowest levels started to diverge gradually after 17:00 and in the period 21:00–midnight the difference was about 180°. After 17:00 EET, 8.4 m wind weakened and turned to the east-northeast (Fig. 2a), so the observed O_3 decrease and CO_2 increase at this level (Fig. 2b and f) were not related to possible emissions from the smoldering ground at the burned site, neither any of the SMEAR II ground-based aerosol measurements.

3.4 Aerosol at SMEAR II

3.4.1 Size distributions

The time series of aerosol number concentrations, the air ion and aerosol number size distributions, and the concentrations of organics show that even though wind blew from the right direction only for a short time, some distinct smoke peaks could be observed at the aerosol cottage and at the SMEAR II main building where the AMS was operated (Fig. 6). Although the AMS measures the concentrations of organics, sulfate, nitrate, chloride, and ammonium, only the concentrations of organics increased in the plume. The concentration of BC measured with the Aethalometer increased above its baseline values only during the flaming phase (Fig. 6f). The peak 5 min average concentration of 3.4 μg m^{-3} was measured at 08:07 EET. In the AOD tower above the canopy level, the peak 1 min BC concentration of 5.4 μg m^{-3} was measured with the MAAP at 08:02 EET.

In the plumes passing by the aerosol cottage during the smoldering phase, the BC concentrations did not increase at all; in the AOD tower, two 1 min peaks were detected (Fig. 6f).

The time series also shows one of the problems of the analysis. For instance, the sum of all species observed with the AMS is clearly lower than the mass concentration calculated from the number size distributions in the size range $D_p < 600$ nm using a density of 1.5 g cm^{-3}. In addition, some of the peak concentrations observed with the other aerosol instruments were not observed with the AMS at all (Fig. 6). The main reason is that the AMS and the DMPS were in different buildings, and the distance between the two sites is about 100 m. In the case of a near-by smoke plume in low wind speed conditions, the influence of this distance is significant.

The NAIS data show that cluster mode ($D_p < 2$ nm) (Fig. 6e) and intermediate mode (D_p = 2–8 nm) (Fig. 6d) air ion number concentrations decreased significantly in the strongest smoke plumes, based on carbon monoxide and particle volume concentrations, both in the flaming and the smoldering phases, suggesting that the ions were attached to the larger aerosols in the plume. The time series also shows that new particle formation occurred during the morning; at 09:20–09:50 EET, the cluster mode concentrations increased and there was a clear nucleation mode also in the size distribution measured with the DMPS. At this time, all indicators of smoke plume were very low, wind was for a while blowing from the east at all levels (WD = 80–120°) so the data suggest that the formation of new aerosol particles was natural and not due to the prescribed burning.

Particle number and volume size distributions were plotted for five selected times (Fig. 7). At 07:50 EET the smoke from the burning area had not yet reached the measurement station, so it can be as a representative of the "baseline size distribution". In it there were three clear modes both in the number and volume size distributions. In the former a nucleation mode at 12 nm, an Aitken mode at 79 nm and an accumulation mode at 223 nm, in the latter an Aitken mode at 106 nm, an accumulation

mode at 264 nm and a coarse mode at 3.6 µm. The integrated mass concentration was 9.4 µg m^{-3} for $D_p < 10$ µm.

The size distribution at 08:00 EET is the clearest one obtained from the smoke plume during the flaming phase. In the number size distribution, there were four modes, the largest of which was at D_g = 80 nm. The geometric standard deviations, i.e., the widths of the modes were quite small, ranging from 1.15 to 1.25 so the fitting was done also by assuming that instead of the three largest modes these comprise one large mode with D_g = 81 nm, σ_g = 1.58 (the dashed line at 08:00). In the volume size distribution there were four modes, the highest concentration of which was at at D_g = 153 nm. The integrated mass concentration was 21.6 µg m^{-3}, the highest during the flaming phase.

At 09:20 EET, there was a very clear nucleation mode at D_g = 8.8 nm, simultaneously with the high positive and negative air ion concentration in the sub-10 nm size range (Fig. 6). At this time, the number concentrations in the Aitken and accumulation modes were lower than in the smoke plume size distribution at 08:00 EET and not very different from those in the "background size distribution" at 07:50 EET, and the mass concentration of 8.9 µg m^{-3} was actually lower than at 07:50 EET. Therefore, it is reasonable to interpret this size distribution as representing natural new particle formation that is frequently observed at SMEAR II during sunny days (dal Maso et al., 2005).

The size distribution at 12:40 EET was measured from the thickest smoke plume arriving at the aerosol cottage during the smoldering phase. This time is when the CO reached the maximum value (Fig. 2e), so the timing of these maxima suggests that this part of the otherwise very patchy plume was wide. In this size distribution, the integrated mass concentration of 28.6 µg m^{-3} was the largest observed in the aerosol cottage during the experiment. In this number size distribution, the largest mode was at D_g = 79 nm, essentially at the same size as in the flaming-phase-plume size distribution at 08:00 EET, but the accumulation mode D_g = 244 nm was larger than that in the flaming phase size distribution. The volume size distribution at 12:40 EET was clearly different from that during the flaming phase at 08:00 EET. First, the mode with the largest concentration was at D_g = 318 nm whereas at 08:00 EET, it was at D_g = 153 nm. Sec-

ond, in the smoldering-phase-plume volume size distribution, the contribution of the coarse-mode particles was much higher than in the flaming-phase-plume size distribution. Actually, the broad shape of the supermicron size distribution and the high $\sigma_g = 2.4$ suggest there were even more modes in the coarse sizes.

At 13:40 EET, another smoke plume was observed at the aerosol cottage, again simultaneously with a CO peak in the mast. The number size distribution was more narrow with the largest mode at $D_g = 122$ nm. The volume size distribution also had two clear accumulation modes and a broad coarse particle size distribution. The fast passage of the smoke plume creates uncertainty to the modal parameters since the smoke plume passages were shorter than the time used for scanning one size distribution. Nevertheless, in both of the size distributions that were measured during the smoldering phase, the mass size distribution had much larger modes than during the flaming phase.

3.4.2 Aerosol optical characterization

In the first smoke plume observed during the flaming phase, light scattering coefficient (σ_{sp}) at $\lambda = 550$ nm was 127 Mm^{-1} (Fig. 8). Because the mass concentrations obtained from the combined DMPS + APS data are available every 10 min, scattering data, which are available at 5 min intervals, were averaged over 10 min for comparison. The peak σ_{sp} in the first smoke plume passage was 93.8 Mm^{-1}, whereas the mass concentration in the size range $D_p < 10$ µm was 21.6 µg m^{-3} (Fig. 7, volume size distribution at 08:00 EET), which yields a mass scattering efficiency of 4.3 $m^2\,g^{-1}$. The highest 5 min-averaged σ_{sp} 137 Mm^{-1} was observed in the smoldering phase at the time the mass concentration reached the maximum value of 28.6 µg m^{-3} (Fig. 7). The corresponding 10 min-averaged $\sigma_{sp} = 116.5$ Mm^{-1} resulted in a mass scattering efficiency of 4.1 $m^2\,g^{-1}$. These mass scattering efficiencies are somewhat higher than the value of 3.1 ± 0.9 $m^2\,g^{-1}$ that was obtained from the 3 yr time series at SMEAR II (Virkkula

et al., 2011), and the median value for the whole burning day that was also 3.1 $m^2\,g^{-1}$, but in good agreement with other published values (e.g., Malm and Hand, 2007).

Light scattering increased when the smoke plume passed the aerosol cottage but the absorption coefficient increased only during two short periods in the flaming phase (Fig. 8a). This is somewhat strange because BC is one of the main products of incomplete combustion. The aerosol was not very dark: the single-scattering albed ω_0 is about 0.3 for pure BC (e.g., Mikhailov et al., 2006) but during the experiment the lowest ω_0 was about 0.7 and in the strongest plume during the flaming phase 0.82. During the smoldering phase ω_0 was ≈ 0.9 and did not deviate from the background values during the smoke plumes (Fig. 8b).

In general the backscatter fraction b of larger particles is smaller than that of smaller particles so the size relationship of the backscatter fraction b is qualitatively similar to that of the Ångström exponent of scattering, α_{sp}. This was also observed in the smoke plumes. There were clear differences in α_{sp} and b between the flaming and smoldering phases; both parameters were clearly lower in the smoke plumes observed during the latter phase (Fig. 8). In the plumes during the flaming phase, the average α_{sp} and b were 2.25 ± 0.01 and 0.171 ± 0.001, respectively, and in the smoldering phase 1.56 ± 0.07 and 0.134 ± 0.001, respectively. These observations and the higher contribution of coarse-mode particles in the smoldering phase (Fig. 7) than in the flaming phase are in line with the general picture of the size relationships of both α_{sp} and b. The two parameters were especially well correlated during the smoldering phase (Fig. 9).

The single-scattering albedo and the backscatter fraction were used for estimating the radiative forcing efficiency dF/δ from Eq. (7). dF/δ is negative for dark surface ($R_s = 0.15$) both during the flaming and smoldering phases, even for the darkest aerosol during the flaming phase (Fig. 8d). For R_s also the value of 0.85 was used to assess the effect of the aerosols above snow surfaces. There the observed aerosol would have a positive radiative forcing (Fig. 8d). The flaming-phase aerosol would heat the atmosphere much stronger than the smoldering phase aerosol.

To estimate the direct radiative forcing dF/δ should be multiplied by the aerosol optical depth δ. However, we do not have any measurement data on the smoke plume optical depth. The sunphotometer that was in the tower east of the aerosol cottage did not detect the smoke at all even though the MAAP that was at the same location did. The main reason is that the most of the smoke plume did not flow between the sunphotometer and the Sun. Another reason is that the sunphotometer made one instantaneous measurement every 15 min according to AERONET (AErosol RObotic NETwork) settings and the smoke plume passed by the mast only during short 1–2 min periods (Fig. 6).

3.5 Organic trace gases

The time series of selected VOCs measured with PTR-MS at the two locations described in Sect. 2.3.1 are plotted together with the CO data from the mast in Fig. 10. The PTR-MS unit that operated in the REA cottage and took its sample from above the canopy sampled some of the clearest smoke plume passages during the flaming phase, but no data were available after 12:00 EET when the smoke plumes with the high CO and aerosol mass concentration during the smoldering phase at 12:40–12:50 EET were detected with the aerosol physical instruments. The unit at the SMEAR II main building that took its sample air from 10 m above ground level did not detect most of the plumes. This was probably caused partly by the unfavourable wind directions in terms of their detection at this station, partly by the substantial meandering of the smoke plumes. Below we only discuss the VOCs measured with the unit in the REA cottage.

Because CO provides the best evidence of burning among the trace gases, we compare it to the VOC data, even though they were not measured exactly at the same location. During the flaming phase there were three clear CO peaks detected in the mast almost simultaneously as the PTR-MS detected high concentrations of several VOCs. The CO and VOC peaks 1–3 in Fig. 10 were not exactly at the same time but they were considered here to be close enough to associate them with each other. In

addition, even the shape of peak 1 over 9 min is very similar for CO and several of the VOCs. So, these data points together with the peaks 2 and 3 were used for calculating linear regressions of ΔX vs. ΔCO where ΔX is the concentration of VOC X over the baseline, as explained above for CO. The scatter plots with the regressions for the 12 compounds with the highest correlation coefficients are shown in Fig. 11. The regessions were calculated twice: both with and without forcing the offset to zero, to give an indication of the uncertainty associated with the ratio. The results are presented in Table 3 where also the uncertainties of the slopes and offsets are shown. The highest correlation coefficients with CO were obtained for m/z associated to methacrolein and furan, the lowest for homosalate – even a negative r value – and monoterpene oxidation products.

The ΔVOC-to-ΔCO ratios cannot be used as emission factors of emitted VOC per mass of burned biomass, but they can be compared to other published data. Andreae and Merlet (2001) presented the emission factors of several trace gases and aerosols of burned dry biomass in various types of forests. For extratropical forests, Andreae and Merlet (2001) gave emission factors for CO of $107 \pm 37\,g\,kg^{-1}$. For furan, the emission factor was 0.40–0.45 $g\,kg^{-1}$ (Andreae and Merlet, 2001), so the ratio 0.425/107 would be 0.004. Values of those ratios in Andreae and Merlet (2001) that could be calculated from our data are presented in Table 3. For some compounds, for instance toluene and acetic acid this ratio in our data is similar to that in Andreae and Merlet (2001), but, for some compounds, for instance dimethylfuran, acetaldehyde, and acetonitrile this ratio is about an order of magnitude larger in our data.

3.6 Observations on mobile platforms

There were three different types of mobile measurements: the research aircraft, *Sniffer*, and the portable particle counters. Here we discuss observations that were aimed at studying the horizontal and vertical dispersion of particles.

Three research flights were conducted during the day. The flight plan was to fly through the smoke plume at several altitudes up to about 3000 m a.g.l. The first flight

was flown during the flaming phase, the second flight was flown during the clear smoldering phase, and the last flight was flown when no smoke was observed on the ground.

During flight 1 (07:40–10:15 EET), elevated particle number and carbon dioxide concentrations indicated the smoke plume up to an altitude of about 1500 m above mean sea level (a.m.s.l.; Fig. 12). This altitude was 200 m lower than the stable layer (i.e., where the virtual potential temperature θ_v increased) in the routine meteorological sounding at the Tikkakoski airport in Jyväskylä, about 90 km northeast from Hyytiälä, at 08:00 EET at the beginning of the flaming phase. So, the smoke rose up to about the top of the boundary layer, but not above it. We flew through the smoke plume at several altitudes and analyzed the 27 clearest plume passages and determined the plume width from the particle number concentration data. This analysis is found in the companion paper by Virkkula et al. (2013).

During flight 2 (11:05–13:40 EET), the boundary layer depth had increased to about 2300 m a.m.s.l. according to the sounding at the Jokioinen Observatory at 14:00 EET (Fig. 12). We observed elevated number concentrations at 2000 m a.m.s.l., but CO_2 concentrations did not exceed background concentrations at any level. During flight 3 (15:50–17:55 EET), particle number concentrations exceeded background concentrations up to about 1000 m a.m.s.l. but CO_2 concentration did not rise above the background concentration.

The horizontal dispersion of the smoke plume is visualized by plotting the concentrations measured with the portable CPCs on the ground and in the aircraft as a function of the latitude and longitude. For the ground level measurements, Fig. 13a shows the paths the pedestrians walked and the concentrations at those locations where the concentration was larger than 10 000 particles cm^{-3}. For the airborne measurements, Fig. 13b shows the locations, the maximum concentrations and the widths of the plumes in the 27 plume passages mentioned above. Both at ground level and aloft, the plume was transported in the direction of the average wind direction at 73 m in elevation measured at the SMEAR II mast.

The location and concentration data were used to estimate the decrease of the concentrations as a function of the distance from the center of the burn area, both in the aircraft and on ground (Fig. 14). The three-dimensional distance was calculated from the center of the burn area to the point location of the measurement. The pedestrian data were arranged in "100 m distance bins" and the maximum of each of these was used for the calculations. The three data points from the *Sniffer* van are the average particle number concentrations over 3–5 min at the distances of 120 m, 180 m and 250 m downwind from the edge of the burned area. For the airborne data, the maxima of each plume passage were used.

The highest particle number concentration, 1.6×10^6 cm^{-3}, was measured with the ELPI in *Sniffer* at 120 m from the burn area. The highest particle number concentration from the research aircraft, 0.94×10^6 cm^{-3}, was measured at the altitude of 118 m a.g.l. The concentration was probably higher, because the particle counter used in the study saturates at 1×10^6 cm^{-3}. The portable CPC model 3007 used by the pedestrians may also have been saturated, with saturation at 1×10^5 cm^{-3} and, with the diluters, up to $\sim 3 \times 10^5$ cm^{-3} was the maximum concentration measured. The maximum 1 min particle number concentration in the aerosol cottage during the experiment was 3.3×10^4 cm^{-3}, an order of magnitude lower than the maxima measured by the pedestrians at some hundreds of meters further away from the burning area.

To get a quantitative estimate of the decrease of the number concentrations, an exponential function $N = N_0 e^{-kx}$ was fitted to the data, where N_0 is the background concentration and x is the distance from the center of the burn area, and k is the reciprocal of the e-folding distance k^{-1}. The fittings yielded e-folding distances of 98 m, 417 m, and 833 m for the *Sniffer*, walker, and aircaft data, respectively. The background particle number concentration at SMEAR II on that day was in the range 1000–3000 cm^{-3} (Fig. 6). This background concentration was reached at ~ 2 km from the burn area at graound level and at ~ 5 km from the burn area in the airborne measurements. However, the exponential form did not fit quite as well to the aircraft data as a power law $N_0 x^{-b}$ within approximately 1 km distance from the burn area (Fig. 14). This suggests

that a Gaussian formula is not necessarily the best option for describing the dilution of smoke in the immediate vicinity of forest fires.

3.7 Changes in soil properties, greenhouse gas and VOC fluxes

The clear-cut and burning of slash increased soil temperature and moisture, soil pH, and NH_4-N and NO_3-N concentrations (Kulmala et al., 2013). The increase in the topsoil soil pH and mineral nitrogen concentrations (NH_4-N and NO_3-N) were rapid, response times being from days to few months, whereas the changes in the deep-soil pH and nitrogen contents were much smaller and were observed with a delay of one to two years. Distinct was that the total available nitrogen concentration did not increase after the clear-cut and burning, but the proportion of mineral nitrogen (NH_4-N and NO_3-N) of the total increased dramatically (Kulmala et al., 2013).

The rates of soil CO_2 efflux at the three sites prior to the clear-cut and burning were similar, but after the treatment, the efflux decreased approximately to half of the flux (Kulmala et al., 2013). Two years later, the difference between the burned clear-cut and the mature control forest decreased. The cumulative soil CO_2 emissions during 2009–2011, interpolated from the chamber measurements and excluding winter months, were the highest at the clear cut but not burned site. Nevertheless, taking into account the rapid CO_2 release during the burning, the burned clear cut site had the highest CO_2 emissions over the 3 yr period (Kulmala et al., 2013)

Before and after the clear-cut and burning, the all the three sites acted as CH_4 sinks. Similar to the CO_2 exchange, the soil uptake of CH_4 decreased significantly soon after the burning. Burning did not seem to have a long-term effect on soil CH_4 uptake as the differences between the three sites disappeared during the following years (Kulmala et al., 2013). The decrease in soil CH_4 uptake after clear-cutting and burning may be related to the increased soil NH_4-N content, as mineral nitrogen in the soil may inhibit CH_4 oxidation (Maljanen et al., 2006; Saari et al., 1997, 2004).

The soil VOC emissions were generally low compared to emissions from similar forest ecosystems. The VOC fluxes between the chambers differed greatly at the burned

site, which is a phenomena often observed with forest-floor VOC flux measurements (Aaltonen et al., 2011). After one year, the emissions of VOCs were nearly stabilized close to the level before the burning.

4 Summary and conclusions

The general goal of the prescribed forest burning experiment experiment on 26 June 2009 in Hyytiälä, Finland, was to collect data for estimating the effect of natural forest fires on air quality and climate. The experiment was designed from the beginning to be multidisciplinary and it had several more detailed goals: to obtain emission factors of aerosols and gases from boreal wildfires, characterization of the climatically relevant physical properties of the smoke aerosol, quantification of the connections between ground-based smoke observations and satellite remote sensing, obtain data for testing an improving modeling of atmospheric dispersion of the fire plume, to study the recovery of the forest after burning, and quantification of the changes taking place in soil carbon stocks and greenhouse gas fluxes following clear-cutting and prescribed burning.

In the campaign a 0.81 ha region of forest near the SMEAR II was cut clear and some tree trunks, all tree tops and all branches were left on the ground and burned. The amount of burned organic material was estimated to be about 46.8 t (i.e., about 60 t ha^{-1}), of which 64 % consisted of the cut tree material, 32 % of organic litter and hummus layer and 4 % of surface vegetation. During the burning, various measurements were conducted on the ground with both fixed and mobile instrumentation, and from a research aircraft. Most of the time the smoke was not transported to the SMEAR II station. This was caused by the low wind speed or calm meteorological conditions that were associated with substantial, sudden variations of the wind direction. The low wind speeds in combination with the substantial buoyancy of the fire plumes resulted in an almost vertical rise of a substantial fraction of the effluents. The fire was started when the wind was from the right direction in terms of the main measuring stations,

but the wind direction soon turned. The ideal wind direction to bring smoke to SMEAR II would have been $190 \pm 10^{\circ}$ whereas the average wind direction was 134–140° at all levels of the SMEAR II 73 m mast. Therefore, the smoke plumes were located west of the station, and the smoke reached the instruments at SMEAR II only during short periods.

Despite of the wind turn we got plenty of data both from within the burn area and outside of it. In the middle of the burning area, CO_2 concentration peaks were around 2000–3000 ppm above the baseline, and peak vertical flow velocities were $6 \pm 3\,m\,s^{-1}$. The meteorological stations placed near the perimeter of the burn area produced data for the analysis of fire dynamics. A strong rise in moisture was observed in the the plume which has been suggested to possibly modify plume dynamics.

The concentrations of the trace gases O_3, NO_x, SO_2, CO and CO_2, which are routinely measured from six different altitudes in the mast, should be elevated in a biomass burning plume. The most distinct exceedances above the background values were for CO, NO_x, and SO_2, but no obvious smoke-plume-related variations were observed for O_3 and CO_2. The lack of a signal in the CO_2 measurements may indicate that the sensitivity or the response time of the CO_2 monitor was not sufficient. Even though the CO_2 concentrations did not rise there were several other indicators of smoke arriving from the burning biomass: elevated particle number concentrations, higher scattering coefficients, elevated CO concentrations, and elevated concentrations of many VOCs that are known to be emitted during biomass burning. They were detected almost simultaneously with the elevated CO concentrations, so linear regressions were calculated between excess concentrations of VOCs and CO. The highest correlations were for methacrolein and furan. For some compounds the ratio to excess CO was very similar to those presented by Andrea and Merlet (2000) but for dimethylfuran, acetaldehyde, and acetonitrile it was an order of magnitude larger.

Peak particle number concentrations were approximately $1–2 \times 10^6\,cm^{-3}$ in the plume at the distance of 100–200 m from the burn area on the ground and in the research aircraft. At SMEAR II the total particle number concentrations increased from ∼ 1000–

$2000\,cm^{-3}$ before the smoke arrived at the instrumentation to $\sim 30\,000\,cm^{-3}$ within the plume. The air ion measurements showed that cluster-mode and intermediate mode ions were depleted in the strongest smoke plume passages, suggesting that the ions were attached to the larger aerosols in the plume. The maximum particle mass concentrations in the smoke plume observed in the aerosol cottage were $21.6\,\mu g\,m^{-3}$ and $28.6\,\mu g\,m^{-3}$ during the flaming and smoldering phases, respectively. In the number size distribution, there were 3–4 modes. The geometric mean diameter of the mode with the highest concentration was at 80 ± 1 nm during the flaming phase and in the middle of the smoldering phase but at the end of the smoldering phase the largest mode was at 122 nm. In the volume size distributions geometric mean diameter of the largest volume mode was at 153 nm during the flaming phase and at 300 nm during the smoldering phase. There were also large supermicron particle modes during the smoldering phase. The main constituent forming the smoke aerosol was organics. The particles were not dark, the lowest single-scattering albedo of the ground-level measurents was 0.7 in the flaming-phase plume and ∼ 0.9 in the smoldering phase. The radiative forcing efficiency was negative above dark surfaces, in other words, the particles cool the atmosphere but when the smoke aerosol gets transported over snow the radiative forcing efficiency becomes positive.

There were changes in soil physical and chemical properties, which influenced the soil greenhouse gas (CO_2, CH_4) fluxes for several years after the burning. The VOC fluxes were generally low and consist mainly on monoterpenes, but clear peak was observed after the burning. One year after the burning, the fluxes were nearly stabilised close to the level before the burning.

The discussion above shows that some of the goals of the experiment were reached, some not. The emission factors of aerosols and gases could not be obtained because most of the smoke did not reach the instrumentation. The climatically relevant physical properties of the smoke aerosol were partially obtained but the lack of aerosol optical depth data and hygroscopic growth factors restrict the estimation of the smoke aerosol climate forcing effect. The quantification of the connections between ground-

based smoke observations and satellite remote sensing failed because the smoke was not detected in any satellite images. The successful part is that we obtained data for testing and improving modeling of atmospheric dispersion of the fire plume, data on the recovery of the forest after burning, and data of the changes taking place in soil carbon stocks and greenhouse gas fluxes following clear-cutting and prescribed burning.

The data will be utilized further. The measurements within the burning area will be used for a spectral analysis of the turbulence within the plume, comparison of the interior tower with the perimeter weather stations, determining the convergence of air from outside the burn perimeter to the center of the plume, and determining the fire-induced winds. The ground-based and airborne measurements are presently used for evaluating and further development of a plume-rise model.

The experiment has taught an important lesson: in the future, we would recommend to use more widely various mobile platforms, in order to be able to measure the fire plumes even in case of rapidly changing wind directions.

Acknowledgements. The financial support by the Academy of Finland as part or the Centre of Excellence program (project no 1118615) and as part of the IS4FIRES project (decision no 122870) is gratefully acknowledged. The experiment was also supported by the European Commission 6th Framework Program Project (EUCAARI), contract 036833-2, European Research Council, University of Helsinki, Finnish Meteorological Institute, Academy of Finland, the TEKES (project KASTU, decision no. 40208/08 and KASTU-2, decision no. 40393/10), San José State University, CA, USA, and Institute for Tropospheric Research, Leipzig, Germany. JP was funded by Academy of Finland project number 218094. Partial funding for DS came from Vaisala Oyj.

References

Aalto, P., Hämeri, K., Becker, E., Weber, R., Salm, J., Mäkelä, J. M., Hoell, C., O'Dowd, C. D., Karlsson, H., Hansson, H.-C., Väkevä, M., Koponen, I. K., Buzorius, G., and Kulmala, M.: Physical characterization of aerosol particles during nucleation events, Tellus B, 53, 344–358, 2001.

Aaltonen, H., Pumpanen, J., Pihlatie, M., Hakola, H., Hellén, H., Kulmala, L., Vesala, T., and Bäck, J.: Boreal pine forest floor biogenic volatile organic compound emissions peak in early summer and autumn, Agr. Forest Meteorol., 151, 682–691, 2011

Achtemeier, G. L.: Measurements of moisture in smoldering smoke and implications for fog, Int. J. Wildland Fire, 15, 517–525, 2006.

Akagi, S. K., Yokelson, R. J., Wiedinmyer, C., Alvarado, M. J., Reid, J. S., Karl, T., Crounse, J. D., and Wennberg, P. O.: Emission factors for open and domestic biomass burning for use in atmospheric models, Atmos. Chem. Phys., 11, 4039–4072, doi:10.5194/acp-11-4039-2011, 2011.

AMAP: The Impact of Black Carbon on Arctic Climate, Arctic Monitoring and Assessment Programme, Oslo, 72 pp., 2011.

Andreae, M. O.: Biomass burning: its history, use, and distribution and its impact on environmental quality and global climate, in: Global Biomass Burning – Atmospheric, Climatic, and Biospheric Implications, edited by: Levine, J. S., MIT Press, Cambridge, MA, 3–21, 1991.

Andreae, M. O. and Merlet, P.: Emission of trace gases and aerosols from biomass burning, Global Biogeochem. Cy., 15, 955–966, 2001.

Andrews, E., Sheridan, P. J., Fiebig, M., McComiskey, A., Ogren, J. A., Arnott, P., Covert, D., Elleman, R., Gasparini, R., Collins, D., Jonsson, H., Schmid, B., and Wang, J.: Comparison of methods for deriving aerosol asymmetry parameter, J. Geophys. Res., 111, D05S04, doi:10.1029/2004JD005734, 2006.

Arnott, W. P., Hamasha, K., Moosmüller, H., Sheridan, P. J., and Ogren, J. A.: Towards aerosol light-absorption measurements with a 7-wavelength aethalometer: evaluation with a photoacoustic instrument and 3-wavelength nephelometer, Aerosol Sci. Tech., 39, 17–29, 2005.

Asmi, E., Sipilä, M., Manninen, H. E., Vanhanen, J., Lehtipalo, K., Gagné, S., Neitola, K., Mirme, A., Mirme, S., Tamm, E., Uin, J., Komsaare, K., Attoui, M., and Kulmala, M.: Results of the first air ion spectrometer calibration and intercomparison workshop, Atmos. Chem. Phys., 9, 141–154, doi:10.5194/acp-9-141-2009, 2009.

Bowman, D. M. J. S., Balch, J. K., Artaxo, P., Bond, W. J., Carlson, J. M., Cochrane, M. A., D'Antonio, C. M., DeFries, R. S., Doyle, J. C., Harrison, S. P., Johnston, F. H., Keeley, J. E., Krawchuk, M. A., Kull, C. A., Marston, J. B., Moritz, M. A., Prentice, I. C., Roos, C. I., Scott, A. C., Swetnam, T. W., van der Werf, G. R., and Pyne, S. J.: Fire in the earth system, Science, 324, 481–484, 2009.

Clements, C. B., Potter, B. E., and Zhong, S.: In situ measurements of water vapor, heat and CO_2 fluxes within a prescribed grass fire, Int. J. Wildland Fire, 15, 299–306, 2006.

Clements, C. B., Zhong, S., Goodrick, S., Li, J., Bian, X., Potter, B. E., Heilman, W. E., Charney, J. J., Perna, R., Jang, M., Lee, D., Patel, M., Street, S., and Aumann, G.: Observing the dynamics of wildland grass fires: FireFlux – a field validation experiment, B. Am. Meteorol. Soc., 88, 1369–1382, 2007.

Clements, C. B., Zhong, S., Bian, X., Heilman, W., and Byun, D.: First observations of turbulence generated by grass fire, J. Geophys. Res., 113, D22102, doi:10.1029/2008JD010014, 2008.

Coen, J., Mahalingam, S., and Daily, J.: Infrared imagery of crown-fire dynamics during FROST-FIRE, J. Appl. Meteorol., 43, 1241–1259, 2004.

Dal Maso, M., Kulmala, M., Riipinen, I., Wagner, R., Hussein, T., Aalto, P. P., and Lehtinen, K. E. J.: Formation and growth of fresh atmospheric aerosols: eight years of aerosol size distribution data from SMEAR II, Hyytiälä, Finland, Boreal Environ. Res., 10, 323–336, 2005.

de Gouw, J. and Warneke, C.: Measurements of volatile organic compounds in the Earth's atmosphere using proton-transfer-reaction mass spectrometry, Mass Spectrom. Rev., 26, 223–257, 2007.

Delene, D. J. and Ogren, J. A.: Variability of aerosol optical properties at four North American surface monitoring sites, J. Atmos. Sci., 59, 1135–1150, 2002.

Drewnick, F., Hings, S. S., DeCarlo, P., Jayne, J. T., Gonin, M., Fuhrer, K., Weimer, S., Jimenez, J. L., Demerjian, K. L., Borrmann, S., and Worsnop, D. R.: A new time-of-flight aerosol mass spectrometer (TOF-AMS) – instrument description and first field deployment, Aerosol Sci. Tech., 39, 637–658, 2005.

Finnish Forest Research Institute: Yearbook of Forest Statistics 1990–1991, Vantaa, Finland, 1992.

Finnish Forest Research Institute: Finnish Statistical Yearbook of Forestry 2011, Vantaa, Finland, 2012.

Flagan, R. C. and Seinfeld, J. H.: Fundamentals of Air Pollution Engineering, Prentice Hall, Englewood Cliffs, NJ, 1988.

Flannigan, M. D. and Haar, T. V.: Forest fire monitoring using NOAA satellite AVHRR, Can. J. Forest Res., 16, 975–982, 1986.

French, N. H., Kasischke, E. S., Hall, R. J., Murphy, K. A., Verbyla, D. L., Hoy, E. E., and Allen, J. L.: Using Landsat data to assess fire and burn severity in the North American boreal forest region: an overview and summary of results, Int. J. Wildland Fire, 17, 443–462, 2008.

Goldammer, J. G. and Furyaev, V. V.: Fire in ecosystems of boreal Eurasia: ecological impacts and links to the global system, in: Fire in Ecosystems of Boreal Eurasia, edited by: Goldammer, J. G. and Furyaev, V. V., Kluwer Acad., Norwell, Mass., 1–20, 1996.

Grell, G., Freitas, S. R., Stuefer, M., and Fast, J.: Inclusion of biomass burning in WRF-Chem: impact of wildfires on weather forecasts, Atmos. Chem. Phys., 11, 5289–5303, doi:10.5194/acp-11-5289-2011, 2011.

Hari, P. and Kulmala, M.: Station for measuring ecosystem–atmosphere relations (SMEAR II), Boreal Environ. Res., 10, 315–322, 2005.

Haywood, J. M. and Shine, K. P.: The effect of anthropogenic sulfate and soot aerosol on the clear sky planetary radiation budget, Geophys. Res. Lett., 22, 603–606, 1995.

Heikinheimo, O.: Kaskiviljelyksen vaikutus Suomen metsiin, Acta Forestalia Fennica, 4, 1–264, 1–149, 1915 (in Finnish with German summary).

Hewitt, C. N., Hayward, S., and Tani, A.: The application of proton transfer reaction-mass spectrometry (PTR-MS) to the monitoring and analysis of volatile organic compounds in the atmosphere, J. Environ. Monit., 5, 1–7, 2003.

Hobbs, P. V., Sinha, P., Yokelson, R. J., Christian, T. J., Blake, D. R., Gao, S., Kirchstetter, T. W., Novakov, T., and Pilewskie, P.: Evolution of gases and particles from a savanna fire in South Africa, J. Geophys. Res., 108, 1–20, 2003.

Janhäll, S., Andreae, M. O., and Pöschl, U.: Biomass burning aerosol emissions from vegetation fires: particle number and mass emission factors and size distributions, Atmos. Chem. Phys., 10, 1427–1439, doi:10.5194/acp-10-1427-2010, 2010.

Jayne, J. T., Leard, D. C., Zhang, X., Davidovits, P., Smith, K. A., Kolb, C. E., and Worsnop, D. R.:. Development of an aerosol mass spectrometer for size and composition analysis of submicron particles, Aerosol Sci. Tech., 33, 49–70, 2000.

Jimenez, J. L., Jayne, J. T., Shi, Q., Kolb, C. E., Worsnop, D. R., Yourshaw, I., Seinfeld, J. H., Flagan, R. C., Zhang, X., Smith, K. A., Morris, J. W., and Davidovits, P.: Ambient aerosol sampling using the Aerodyne Aerosol Mass Spectrometer, J. Geophys Res., 108, D78425, doi:10.1029/2001JD001213, 2003.

Keskinen, J., Pietarinen, K., and Lehtimäki, M.: Electrical low pressure impactor, J. Aerosol Sci., 23, 353–360, 1992.

Kiefer, C. M., Clements, C. B., and Potter, B. E.: Application of a mini-unmanned aircraft system for in situ monitoring of fire plume thermodynamics properties, J. Atmos. Ocean. Tech., 29, 309–315, 2012

Klein, T., Kukkonen, J., Dahl, Å, Bossioli, E., Baklanov, A., Vik, A. F., Agnew, P., Karatzas, K. D., and Sofiev, M.: Interactions of physical, chemical, and biological weather calling for an integrated approach to assessment, forecasting, and communication of air quality, Ambio, 41, 851–864, doi:10.1007/s13280-012-0288-z, 2012.

Kulmala, L., Pumpanen, J., Pohja, T., Laakso, H., Siivola, E., Hari, P., and Vesala, T.: A Novel automatic chamber to measure soil CO_2 efflux, Rep. Ser. Aerosol Sci., 109, available at: http://www.atm.helsinki.fi/FAAR/reportseries/rs-109/abstracts/Liisa%20Kulmala.pdf (last access: August 2013), 2010.

Kulmala, L., Pumpanen, J., Levula, J., Rantanen, S., Laakso, H., Siivola, E., Kolari, P., and Vesala, T.: CO_2 efflux before and after a clear cut and prescribed burning of a boreal spruce forest, Rep. Ser. Aerosol Sci., 126, 184–187, 2011.

Kulmala, L., Aaltonen, H., Korhonen, J. F. K., Pihlatie, M., Pumpanen, J., Levula, J., and Nikinmaa, E.: Changes in physical and chemical soil properties after a clear cut and prescribed burning of slash in a boreal spruce forest, Rep. Ser. Aerosol Sci., 134, 389–393, 2012.

Kulmala, L., Aaltonen, H., Berninger, F., Kieloaho, A.-J., Levula, J., Bäck, J., Hari, P., Kolari, P., Korhonen J.F.J., Kulmala, M., Nikinmaa, E., Pihlatie, M., Vesala, T., and Pumpanen, J.: Changes in biogeochemistry and carbon fluxes in a boreal forest after the clear-cutting and partial burning of slash, Agricultural and Forest Meteorology, submitted, 2013.

Kulmala, M., Asmi, A., Lappalainen, H. K., Baltensperger, U., Brenguier, J.-L., Facchini, M. C., Hansson, H.-C., Hov, Ø., O'Dowd, C. D., Pöschl, U., Wiedensohler, A., Boers, R., Boucher, O., de Leeuw, G., Denier van der Gon, H. A. C., Feichter, J., Krejci, R., Laj, P., Lihavainen, H., Lohmann, U., McFiggans, G., Mentel, T., Pilinis, C., Riipinen, I., Schulz, M., Stohl, A., Swietlicki, E., Vignati, E., Alves, C., Amann, M., Ammann, M., Arabas, S., Artaxo, P., Baars, H., Beddows, D. C. S., Bergström, R., Beukes, J. P., Bilde, M., Burkhart, J. F., Canonaco, F., Clegg, S. L., Coe, H., Crumeyrolle, S., D'Anna, B., Decesari, S., Gilardoni, S., Fischer, M., Fjaeraa, A. M., Fountoukis, C., George, C., Gomes, L., Halloran, P., Hamburger, T., Harrison, R. M., Herrmann, H., Hoffmann, T., Hoose, C., Hu, M., Hyvärinen, A., Hõrrak, U., Iinuma, Y., Iversen, T., Josipovic, M., Kanakidou, M., Kiendler-Scharr, A., Kirkevåg, A., Kiss, G., Klimont, Z., Kolmonen, P., Komppula, M., Kristjánsson, J.-E., Laakso, L., Laaksonen, A., Labonnote, L., Lanz, V. A., Lehtinen, K. E. J., Rizzo, L. V., Makkonen, R., Man-

ninen, H. E., McMeeking, G., Merikanto, J., Minikin, A., Mirme, S., Morgan, W. T., Nemitz, E., O'Donnell, D., Panwar, T. S., Pawlowska, H., Petzold, A., Pienaar, J. J., Pio, C., Plass-Duelmer, C., Prévôt, A. S. H., Pryor, S., Reddington, C. L., Roberts, G., Rosenfeld, D., Schwarz, J., Seland, Ø., Sellegri, K., Shen, X. J., Shiraiwa, M., Siebert, H., Sierau, B., Simpson, D., Sun, J. Y., Topping, D., Tunved, P., Vaattovaara, P., Vakkari, V., Veefkind, J. P., Visschedijk, A., Vuollekoski, H., Vuolo, R., Wehner, B., Wildt, J., Woodward, S., Worsnop, D. R., van Zadelhoff, G.-J., Zardini, A. A., Zhang, K., van Zyl, P. G., Kerminen, V.-M., S Carslaw, K., and Pandis, S. N.: General overview: European Integrated project on Aerosol Cloud Climate and Air Quality interactions (EUCAARI) – integrating aerosol research from nano to global scales, Atmos. Chem. Phys., 11, 13061–13143, doi:10.5194/acp-11-13061-2011, 2011.

Lamarque, J.-F., Bond, T. C., Eyring, V., Granier, C., Heil, A., Klimont, Z., Lee, D., Liousse, C., Mieville, A., Owen, B., Schultz, M. G., Shindell, D., Smith, S. J., Stehfest, E., Van Aardenne, J., Cooper, O. R., Kainuma, M., Mahowald, N., McConnell, J. R., Naik, V., Riahi, K., and van Vuuren, D. P.: Historical (1850–2000) gridded anthropogenic and biomass burning emissions of reactive gases and aerosols: methodology and application, Atmos. Chem. Phys., 10, 7017–7039, doi:10.5194/acp-10-7017-2010, 2010.

Lavoué, D., Liousse, C., Cachier, H., Stocks, B. J., and Goldammer, J.: Modeling of carbonaceous particles emitted by boreal and temperate wildfires at northern latitudes, J. Geophys. Res., 105, 26871–26890, 2000.

Law, K. S. and Stohl, A.: Arctic air pollution: origins and impacts, Science, 315, 1537, doi:10.1126/science.1137695, 2007.

Lentile, L. B., Holden, Z. A., Smith, A. M., Falkowski, M. J., Hudak, A. T., Morgan, P., Lewis, S. A., Gessler, P. E., and Benson, N. C.: Remote sensing techniques to assess active fire characteristics and post-fire effects, Int. J. Wildland Fire, 15, 319–345, 2006.

Maljanen, M., Jokinen, H., Saari, A., Strommer, R., and Martikainen, P.: Methane and nitrous oxide fluxes, and carbon dioxide production in boreal forest soil fertilized with wood ash and nitrogen, Soil Use Manage., 22, 151–157, 2006.

Malm, W. C. and Hand, J. L.: An examination of the physical and optical properties of aerosols collected in the IMPROVE program, Atmos. Environ., 41, 3407–3427, 2007.

Manninen, H. E., Petäjä, T., Asmi, E., Riipinen, I., Nieminen, T., Mikkilä, J., Hõrrak, U., Mirme, A., Mirme, S., Laakso, L., Kerminen, V.-M., and Kulmala, M.: Long-term field measurements of charged and neutral clusters using Neutral cluster and Air Ion Spectrometer (NAIS), Boreal Environ. Res., 14, 591–605, 2009.

Marjamäki, M., Ntziachristos, L., Virtanen, A., Ristimäki, J., Keskinen, J., Moisio, M., Palonen, M., and Lappi, M.: Electrical Filter Stage for the ELPI, Society of Automotive Engineers (SAE), Technical Paper 2002-01-0055, doi:10.4271/2002-01-0055, 2002.

Mikhailov, E., Vlasenko, S., Podgorny, I., Ramanathan, V., and Corrigan, C.: Optical properties of soot-water drop agglomerates: an experimental study, J. Geophys. Res., 111, 1–16, 2006.

National Interagency Fire Center: Fire information, statistics for prescribed fire and wildland fire use fires, available at: http://www.nifc.gov/fireInfo/fireInfo_statistics.html (last access: 10 December 2012), 2011.

Paris, J.-D., Stohl, A., Nédélec, P., Arshinov, M. Yu., Panchenko, M. V., Shmargunov, V. P., Law, K. S., Belan, B. D., and Ciais, P.: Wildfire smoke in the Siberian Arctic in summer: source characterization and plume evolution from airborne measurements, Atmos. Chem. Phys., 9, 9315–9327, doi:10.5194/acp-9-9315-2009, 2009.

Penner, J. E., Dickinson, R. E., and O'Neill, C. A.: Effects of aerosol from biomass burning on the global radiation budget, Science, 256, 1432–1434, 1992.

Pihlatie, M., Christiansen, J. R., Aaltonen, H., Korhonen, J. F. J., Nordbo, A., Rasilo, T., Benanti, G., Giebels, M., Helmy, M., Sheehy, J., Jones, S., Juszczak, R., Klefoth, R., Lobo do Vale, R., Rosa, A. P., Schreiber, P., Serça, D., Vicca, S., Wolf, B., and Pumpanen, J.: Comparison of static chambers to measure CH_4 emissions from soils, Agr. Forest Meteorol., 171–172, 124–136, 2013.

Pirjola, L., Parviainen, H., Hussein, T., Valli, A., Hämeri, K., Aalto, P., Virtanen, A., Keskinen, J., Pakkanen, T., Mäkelä, T., and Hillamo, R.: "Sniffer" – a novel tool for chasing vehicles and measuring traffic pollutants, Atmos. Environ., 38, 3625–3635, 2004.

Pirjola, L., Paasonen, P., Pfeiffer, D., Hussein, T., Hämeri, K., Koskentalo, T., Virtanen, A., Rönkkö, T., Keskinen, J., Pakkanen, T. A., and Hillamo, R. E.: Dispersion of particles and trace gases nearby a city highway: mobile laboratory measurements in Finland, Atmos. Environ., 40, 867–879, 2006.

Potter, B. E.: The role of released moisture in the atmospheric dynamics associated with wildland fires, Int. J. Wildland Fire, 14, 77–84, doi:10.1071/WF04045, 2005.

Radke, L. F., Hegg, D. A., Hobbs, P. V., Nance, J. D., Lyons, J. H., Laursen, K. K., Weiss, R. E., Riggan, P. J., and Ward, D. E.: Particulate and trace gas emissions from large biomass fires in North America, in: Global Biomass Burning – Atmospheric, Climatic, and Biospheric Implications, MIT Press, Cambridge, Mass, 1991.

Randerson, J. T., Liu, H., Flanner, M. G., Chambers, S. D., Jin, Y., Hess, P. G., Pfister, G., Mack, M. C., Treseder, K. K., Welp, L. R., Chapin, F. S., Harden, J. W., Goulden, M. L., Lyons, E., Neff, J. C., Schuur, E. A. G., and Zender, C. S.: The impact of boreal forest fire on climate warming, Science, 314, 1130–1132, doi:10.1126/science.1132075, 2006.

Reid, J. S., Koppmann, R., Eck, T. F., and Eleuterio, D. P.: A review of biomass burning emissions part II: intensive physical properties of biomass burning particles, Atmos. Chem. Phys., 5, 799–825, doi:10.5194/acp-5-799-2005, 2005a.

Reid, J. S., Eck, T. F., Christopher, S. A., Koppmann, R., Dubovik, O., Eleuterio, D. P., Holben, B. N., Reid, E. A., and Zhang, J.: A review of biomass burning emissions part III: intensive optical properties of biomass burning particles, Atmos. Chem. Phys., 5, 827–849, doi:10.5194/acp-5-827-2005, 2005b.

Repola, J., Ojansuu, R., and Kukkola, M.: Biomass functions for Scots pine, Norway spruce and birch in Finland, Working Papers of the Finnish Forest Research Institute, 53, 28 pp., available at: http://www.metla.fi/julkaisut/workingpapers/2007/mwp053.htm (last access: August 2013), 2007.

Saari, A., Martikainen, P., Ferm, A., Ruuskanen, J., De Boer, W., Troelstra, S., and Laanbroek, H. J.,: Methane oxidation in soil profiles of Dutch and Finnish coniferous forests with different soil texture and atmospheric nitrogen deposition, Soil Biol. Biochem., 29, 1625–1632, 1997.

Saari, A., Rinnan, R., and Martikainen, P. J.: Methane oxidation in boreal forest soils: kinetics and sensitivity to pH and ammonium, Soil Biol. Biochem., 36, 1037–1046, 2004.

Saarnio, K., Aurela, M., Timonen, H., Saarikoski, S., Teinilä, K., Mäkelä, T., Sofiev, M., Koskinen, J., Aalto, P. P., Kulmala, M., Kukkonen, J., and Hillamo, R.: Chemical composition of fine particles in fresh smoke plumes from boreal wild-land fires in Europe, Sci. Total Environ., 408, 2527–2542, 2010.

Saarikoski, S., Sillanpää, M., Sofiev, M., Timonen, H., Saarnio, K., Teinilä, K., Karppinen, A., Kukkonen, J., and Hillamo, R.: Chemical composition of aerosols during a major biomass burning episode over northern Europe in spring 2006: experimental and modelling assessments, Atmos. Environ., 41, 3577–3589, 2007.

Schlesinger, W. H.: Biogeochemistry, an Analysis of Global Change, Academic Press, San Diego, USA, 588 pp., 1997.

Schobesberger, S., Väänänen, R., Leino, K., Virkkula, A., Backman, J., Pohja, T., Siivola, E., Franchin, A., Mikkilä, J., Paramonov, M., Aalto, P. P., Krejci, R., Petäjä, T., and Kulmala, M.:

Airborne measurements over the boreal forest of southern Finland during new particle formation events in 2009 and 2010, Boreal Environ. Res., 18, 145–163, 2013.

Schuster, G. L., Dubovik, O., and Holben, B. N.: Angstrom exponent and bimodal aerosol size distributions, J. Geophys. Res., 111, D07207, doi:10.1029/2005JD006328, 2006.

Sheridan, P. J. and Ogren, J. A.: Observations of the vertical and regional variability of aerosol optical properties over central and eastern North America, J. Geophys. Res., 104, 16793–16805, 1999.

Shindell, D. T., Chin, M., Dentener, F., Doherty, R. M., Faluvegi, G., Fiore, A. M., Hess, P., Koch, D. M., MacKenzie, I. A., Sanderson, M. G., Schultz, M. G., Schulz, M., Stevenson, D. S., Teich, H., Textor, C., Wild, O., Bergmann, D. J., Bey, I., Bian, H., Cuvelier, C., Duncan, B. N., Folberth, G., Horowitz, L. W., Jonson, J., Kaminski, J. W., Marmer, E., Park, R., Pringle, K. J., Schroeder, S., Szopa, S., Takemura, T., Zeng, G., Keating, T. J., and Zuber, A.: A multi-model assessment of pollution transport to the Arctic, Atmos. Chem. Phys., 8, 5353–5372, doi:10.5194/acp-8-5353-2008, 2008.

Simpson, I. J., Akagi, S. K., Barletta, B., Blake, N. J., Choi, Y., Diskin, G. S., Fried, A., Fuelberg, H. E., Meinardi, S., Rowland, F. S., Vay, S. A., Weinheimer, A. J., Wennberg, P. O., Wiebring, P., Wisthaler, A., Yang, M., Yokelson, R. J., and Blake, D. R.: Boreal forest fire emissions in fresh Canadian smoke plumes: C_1–C_{10} volatile organic compounds (VOCs), CO_2, CO, NO_2, NO, HCN and CH_3CN, Atmos. Chem. Phys., 11, 6445–6463, doi:10.5194/acp-11-6445-2011, 2011.

Sofiev, M., Vankevich, R., Lotjonen, M., Prank, M., Petukhov, V., Ermakova, T., Koskinen, J., and Kukkonen, J.: An operational system for the assimilation of the satellite information on wild-land fires for the needs of air quality modelling and forecasting, Atmos. Chem. Phys., 9, 6833–6847, doi:10.5194/acp-9-6833-2009, 2009.

Sullivan, A.: Competitive thermokinetics and nonlinear bushfire behavior, Ph.D. Thesis, Australian National University, 229 pp., 2007.

Taipale, R., Ruuskanen, T. M., Rinne, J., Kajos, M. K., Hakola, H., Pohja, T., and Kulmala, M.: Technical Note: Quantitative long-term measurements of VOC concentrations by PTR-MS – measurement, calibration, and volume mixing ratio calculation methods, Atmos. Chem. Phys., 8, 6681–6698, doi:10.5194/acp-8-6681-2008, 2008.

van der Werf, G. R., Randerson, J. T., Giglio, L., Collatz, G. J., Mu, M., Kasibhatla, P. S., Morton, D. C., DeFries, R. S., Jin, Y., and van Leeuwen, T. T.: Global fire emissions and the

contribution of deforestation, savanna, forest, agricultural, and peat fires (1997–2009), Atmos. Chem. Phys., 10, 11707–11735, doi:10.5194/acp-10-11707-2010, 2010.

van Leeuwen, T. T. and van der Werf, G. R.: Spatial and temporal variability in the ratio of trace gases emitted from biomass burning, Atmos. Chem. Phys., 11, 3611–3629, doi:10.5194/acp-11-3611-2011, 2011.

Virkkula, A., Backman, J., Aalto, P. P., Hulkkonen, M., Riuttanen, L., Nieminen, T., dal Maso, M., Sogacheva, L., de Leeuw, G., and Kulmala, M.: Seasonal cycle, size dependencies, and source analyses of aerosol optical properties at the SMEAR II measurement station in Hyytiälä, Finland, Atmos. Chem. Phys., 11, 4445–4468, doi:10.5194/acp-11-4445-2011, 2011.

Virkkula, A., Schobesberger, S., Pohja, T., Aalto, P., Keronen, P., Backman, J., Petäjä, T., and Kulmala, M.: Airborne measurements of aerosols and carbon dioxide during a prescribed forest burning experiment at a boreal forest site, in preparation, 2013.

Viro, P. J.: Prescribed Burning in Forestry, Communicationes Instituti Forestalis Fenniae, 67, 1969.

Ward, D. E. and Hao, W. M.: Air toxic emissions from burning of biomass globally – preliminary estimates, paper presented at 85th Annual Meeting, Air and Waste Management Association, Vancouver, British Columbia, 1992.

Yli-Ojanperä, J., Kannosto, J., Marjamäki, M., and Keskinen, J.: Improving the nanoparticle resolution of the ELPI, Aerosol Air Qual. Res., 10, 360–366, 2010.

Yokelson, R. J., Griffith, D. W. T., and Ward, D. W.: Open-path Fourier transform infrared studies of large-scale laboratory biomass fires, J. Geophys. Res., 101, 21067–21080, 1996.

Yokelson, R. J., Burling, I. R., Gilman, J. B., Warneke, C., Stockwell, C. E., de Gouw, J., Akagi, S. K., Urbanski, S. P., Veres, P., Roberts, J. M., Kuster, W. C., Reardon, J., Griffith, D. W. T., Johnson, T. J., Hosseini, S., Miller, J. W., Cocker III, D. R., Jung, H., and Weise, D. R.: Coupling field and laboratory measurements to estimate the emission factors of identified and unidentified trace gases for prescribed fires, Atmos. Chem. Phys., 13, 89–116, doi:10.5194/acp-13-89-2013, 2013.

Table 1. Estimated amount of burned organic material during the experiment. s.e. = standard error of the estimate.

	Mass ± s.e. (kg)	Mass/Area ± s.e. ($kg\,ha^{-1}$)	Carbon ± s.e. (kg)	Carbon/Area ± s.e. ($kg\,ha^{-1}$)
Tree Biomass	30 700	38 030	15 400	19 080
Surface vegetation	1850	2300	930	1150
Organic Soil Layer	14 200	17 600	7100	8800
Sum	46 800 ± 10 900	58 000 ± 13 500	23 400 ± 5500	29 000 ± 6800

Table 2. Measurements made during the prescribed forest burning campaing, the instrument type, location of the instrument, and the responsible institute.

Quantity	Intsrument	Location	Institute
Meteorology			
Heat flux	Hukseflux Inc. SBG01	mast within the burn area	SJSU
Temperature	Fine wire thermocouples	mast within the burn area	SJSU
Wind	2-D anemometers	SMR II mast, several altitudes	UHEL
	Vaisala WXT 520	small masts around burn area	FMI
	3-D sonic anemometer, ATI, Sx probe	mast within the burn area	SJSU
Trace gases			
CO_2	URAS 4	SMR II mast, several altitudes	UHEL
		mast within the burn area	SJSU
CO	Horiba APMA	SMR II mast, several altitudes	UHEL
NO_x	TEI 42CTL	SMR II mast, several altitudes	UHEL
O_3	TEI 49C	SMR II mast, several altitudes	UHEL
VOCs	Proton Transfer Reaction Mass Spectrometer (PTR-MS)	REA cottage	UHEL
		SMR II, new part	UHEL
Aerosol physical properties			
Size distribution			
D_p: 3–1000 nm	Differential Mobility Particle Sizer	Aerosol cottage	UHEL
D_p: 0.5–10 µm	Aerodynamic Particle Sizer	Aerosol cottage	UHEL
D_p: 0.4–40 nm	Neutral cluster and Air Ion Spectrometer (NAIS)	Aerosol cottage	UHEL
Scattering coefficient	3-λ nephelometer	Aerosol cottage	UHEL
Absorption coefficient	7-λ aethalometer	Aerosol cottage	UHEL
	Multi-Angle Absorption Photometer (MAAP)	AOD tower	FMI
Aerosol optical depth	Sunphotometer	AOD tower	FMI
Aerosol chemical composition			
NO_3^-	Aerosol Mass Spectrometer (AMS)	SMR II, new part	UHEL
SO_4^{2-}	AMS	SMR II, new part	UHEL
NH_4^+	AMS	SMR II, new part	UHEL
Cl^-	AMS	SMR II, new part	UHEL
Organics	AMS	SMR II, new part	UHEL
Mobile measurements on ground			
Number concentration	3 portable Condensation Particle Counters	Walking	UHEL
Number concentration	Electric Low Pressure Impactor (ELPI)	*Sniffer* van	MUAS
Size distribution		*Sniffer* van	MUAS
CO_2		*Sniffer* van	MUAS
CO		*Sniffer* van	MUAS
NO_x		*Sniffer* van	MUAS
Airborne			
Number concentration	2 TSI Model 3762 and 1 model 3772 CPC	Cessna 172	UHEL
Scattering coefficient	Radiance Research, 1-λ nephelometer, 545 nm	Cessna 172	UHEL
Absorption coefficient	Radiance Research, 3-λ PSAP	Cessna 172	UHEL
CO_2	LICOR LI-84	Cessna 172	UHEL
Soil measurements			
Temperature	iButtons, PT100	Burned and reference area	UHEL
Moisture	ThetaProbe	Burned and reference area	UHEL
pH		Burned and reference area	UHEL
C/N-ratio		Burned and reference area	UHEL
Nitrogen compounds		Burned and reference area	UHEL
CO_2 efflux	Vaisala GMP343	Burned and reference area	UHEL
CH_4 flux	Agilent Gas Chromatograph model 7890A	Burned and reference area	UHEL
VOC flux	Tenax-Carbopack-B + GC-MS	Burned area	UHEL

Table 3. Relationships of excess-concentrations of VOCs (ΔX) to excess carbon monoxide (ΔCO) during the flaming phase. The slopes and offsets and their standard errors (s.e.) are those obtained from a linear regression of ΔX = slope × ΔCO+ offset. The data are sorted according to the correlation coefficient *r*. X/CO: ratio of selected emission factors of VOC X and CO in extratropical biomass burning according to Andrea eand Merlet (2001).

Compound (*m*/*z*)	slope ± s.e.	offset ± s.e.	*r*	X/CO
methacrolein, methyl vinyl ketone (71)	0.0066 ± 0.0007	−0.066 ± 0.036	0.955	
isoprene, methylbutenol fragment, furan (69)	0.0061 ± 0.0008	−0.013 ± 0.040	0.936	0.0040*
butanol, hydroxyacetone (75)	0.0193 ± 0.0028	−0.341 ± 0.147	0.919	
methyl ethyl ketone (73)	0.0119 ± 0.0019	−0.030 ± 0.102	0.900	
dimethylfuran (97)	0.0205 ± 0.0040	−0.444 ± 0.215	0.860	0.0005
2-vinylfuran, phenol (95)	0.0067 ± 0.0014	−0.165 ± 0.073	0.852	
hexenal (99)	0.0119 ± 0.0025	−0.218 ± 0.130	0.850	
acetaldehyde (45)	0.0471 ± 0.0103	−1.336 ± 0.546	0.836	0.0047
formaldehyde (31)	0.0102 ± 0.0023	−0.086 ± 0.121	0.831	0.0206
methylbutenol (87)	0.0130 ± 0.0029	−0.199 ± 0.156	0.827	
toluene (93)	0.0044 ± 0.0010	−0.075 ± 0.054	0.822	0.0037
cis-3-hexenol fragment, hexanal fragment, methylfuran (83)	0.0127 ± 0.0030	−0.187 ± 0.158	0.818	
acetone (59)	0.0070 ± 0.0016	0.235 ± 0.087	0.817	0.0051
hexanol (103)	0.0055 ± 0.0013	−0.100 ± 0.069	0.817	
acetic acid (61)	0.0356 ± 0.0085	−0.234 ± 0.453	0.812	0.0355
cis-3-hexenol, hexanal (101)	0.0145 ± 0.0035	−0.156 ± 0.186	0.810	
methanol (33)	0.0782 ± 0.0190	−1.313 ± 1.011	0.807	0.0187
methyl salicylate (153)	0.0022 ± 0.0005	−0.001 ± 0.029	0.807	
cineol (155)	0.0017 ± 0.0004	−0.102 ± 0.022	0.802	
acetonitrile (42)	0.0133 ± 0.0033	−0.311 ± 0.178	0.798	0.0018
C9-aromatics (121)	0.0022 ± 0.0006	−0.020 ± 0.030	0.797	
monoterpene fragments, hexenal fragment (81)	0.0160 ± 0.0044	−0.157 ± 0.232	0.774	
benzene (79)	0.0123 ± 0.0034	−0.128 ± 0.182	0.768	0.0046
monoterpenes (137)	0.0063 ± 0.0019	0.061 ± 0.102	0.739	
sesquiterpenes (205)	0.0006 ± 0.0003	−0.073 ± 0.015	0.610	
ethanol, formic acid (47)	0.0058 ± 0.0028	0.177 ± 0.149	0.564	
dimethyl sulfide, acetaldehyde-water cluster (63)	0.0006 ± 0.0005	0.014 ± 0.029	0.360	
monoterpene oxidation products (169)	0.0000 ± 0.0007	0.095 ± 0.038	0.004	
homosalate (263)	−0.0007 ± 0.0004	0.015 ± 0.022	−0.488	

* Calculated from the emission factor of furan in Andreae and Merlet (2001).

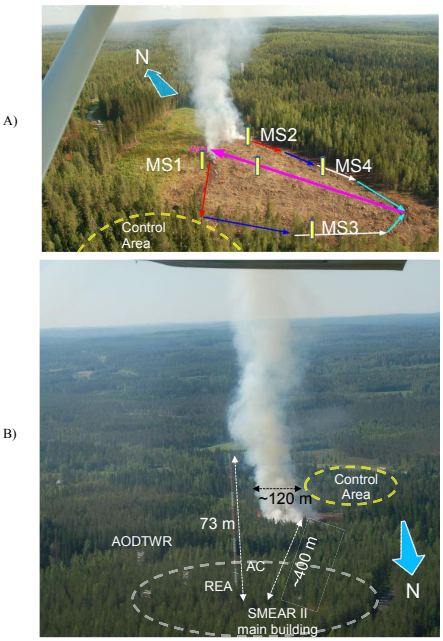

Fig. 1. Aerial photographs of the study site during the flaming phase: **(A)** from the south, with the progress of the ignition described with the red, blue, white, and light blue arrows, and the average wind direction with the pink arrow. The yellow bars denote the poles (not in scale) with meteorological sensors (MS1–MS4) on top. **(B)** From the north at approximately 300 m a.g.l. The majority of the aerosol and gas measurement instrumentation of SMEAR II are located within the white dashed oval. The control area is within the yellow oval. The blue arrow shows the approximate direction to the north. AC: aerosol cottage, REA: relaxed eddy accumulation cottage, AODTWR: Aerosol Optical Depth Tower.

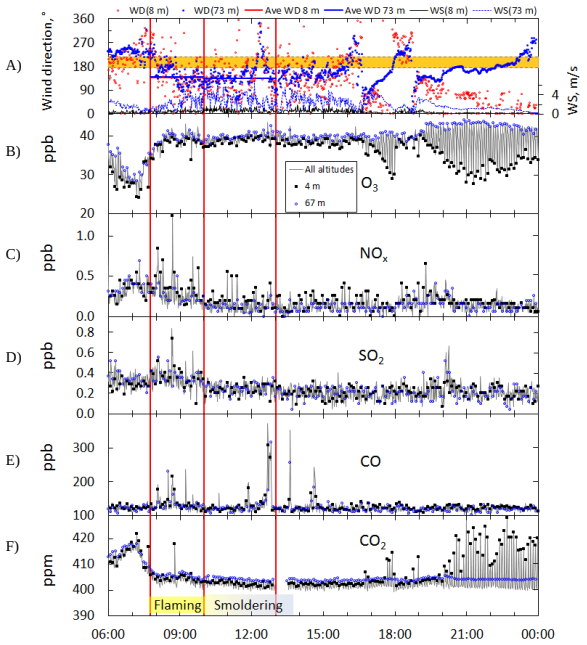

Fig. 2. Selected data obtained from the SMEAR II mast during the burning day at a 1 min time resolution. **(A)** Wind direction and speed at two altitudes: 8 m and 74 m above ground level. The dark yellow shading indicates the wind direction sector that would bring smoke from the fire to SMEAR II. **(B–F)** Concentrations of selected trace gases measured at all altitudes (grey line) and at the lowest and the highest trace gas sampling levels: 4 m and 67 m above ground (black square and blue circle, respectively). The red vertical lines indicate the start and end of the flaming and clear smoldering phases.

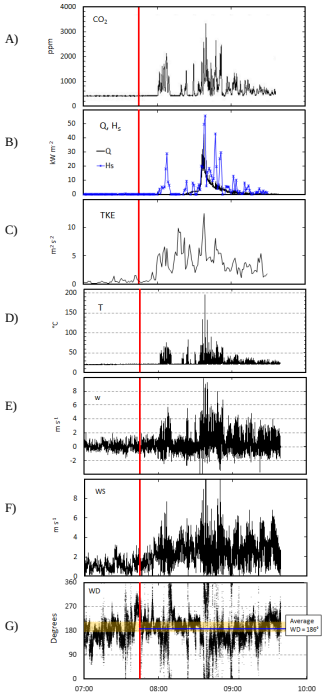

Fig. 3. Observations within the burning area burning area during the flaming phase. **(A)** CO_2 concentrations, **(B)** heat flux (Q), turbulent sensible heat flux (H_s), **(C)** turbulent kineticg energy (TKE), **(D)** temperature (T), and **(E)** vertical flow velocity (w), **(F)** horizontal wind speed (WS), and **(G)** wind direction (WD) at 12 m altitude. The 3-D wind data are at 10 Hz, the others at 1 Hz time resolution. The red line shows the ignition time at 07:45. The yellow shading indicates the wind direction sector that would bring smoke from the fire to SMEAR II.

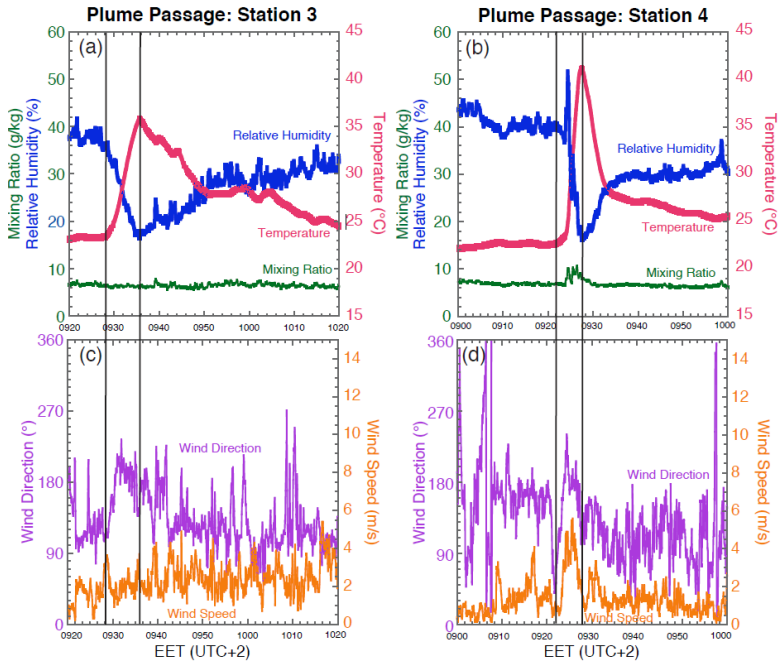

Fig. 4. Observations on top of two meteorological stations outside of the perimeter of the burning area.

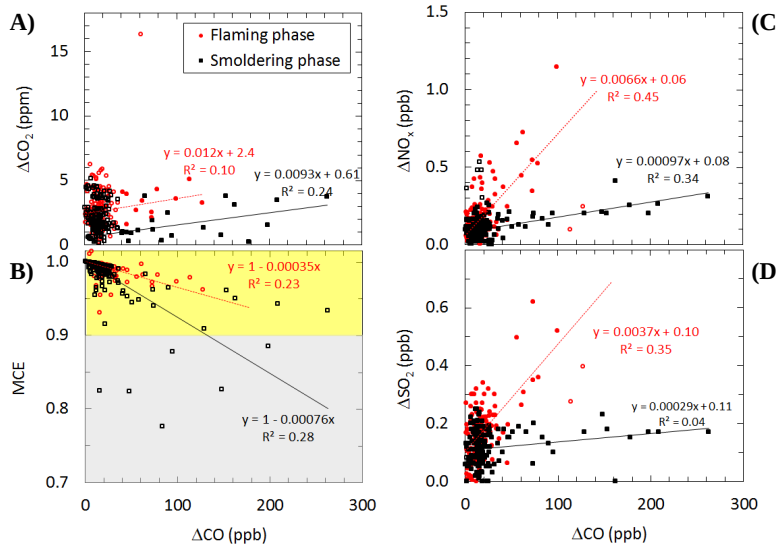

Fig. 5. Relationships of trace gases measured from the SMEAR II mast during the flaming and smoldering phases. Left: **(A)** excess CO_2 and **(B)** modified combustion efficiency as a function of excess CO concentration, right: **(C)** excess NO_x and **(D)** excess SO_2 concentrations as a function of excess CO concentration. The yellow shading in the low left panel denotes the range of MCE values where more than 50 % of combustion can be assumed to be flaming and the grey shading the range of MCE values where more than 50 % of combustion can be assumed to be smoldering.

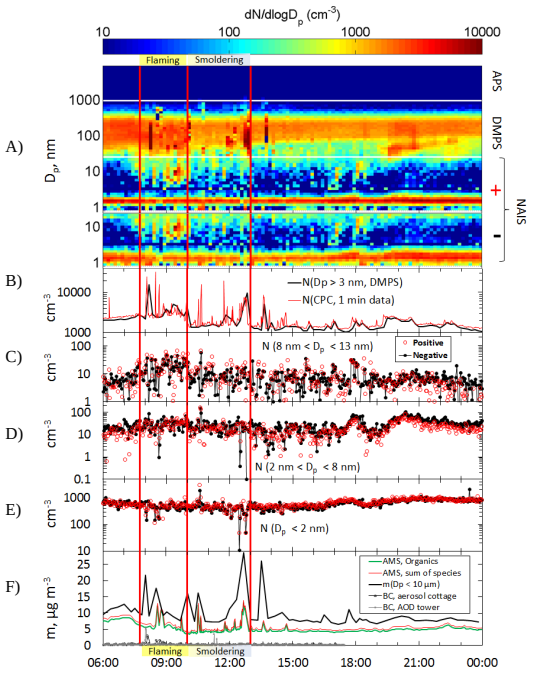

Fig. 6. Data of selected ground-based aerosol measurements at SMEAR II on 26 June 2009. **(A)** Particle number size distributions measured with the APS and the DMPS, and the positive and negative air ion size distributions measured with the NAIS, **(B)** total particle number concentrations measured with a CPC and integrated from the DMPS, **(C–E)** air ion number concentrations from the NAIS data in three different size ranges and **(E)** concentrations of organics and the sum of all compounds measured with an AMS, mass concentration of particles smaller than 10 µm using the density of 1.5 g cm^{-3}, and black carbon concentration at two locations.

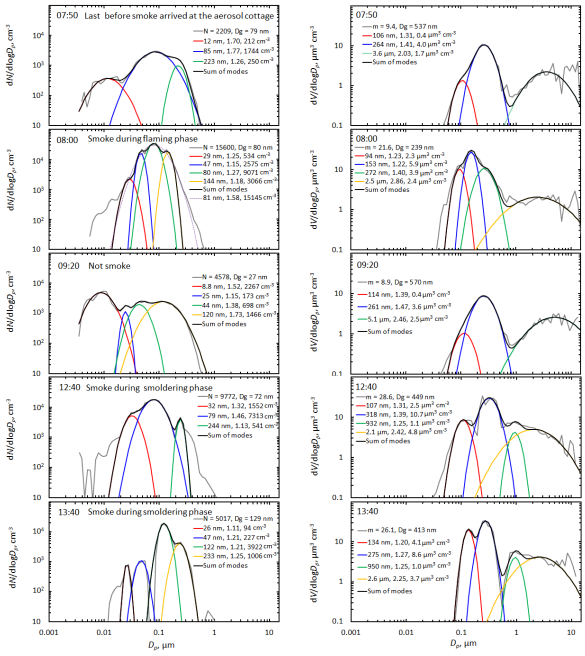

Fig. 7. Selected particle size distributions measured with DMPS and APS in the aerosol cottage. The left column: number size distributions, right column: volume size distributions. In each plot the grey line represents the measured size distribution and the associated numbers the number concentration in cm^{-3} (left column), the mass concentration integrated to 10 µm in µg m^{-3} calculated assuming a density of 1.5 g cm^{-3}, (right column), and the geometric mean diameter (D_g) of the whole size distribution. The modal parameters are the geometric mean diameter, the geometric standard deviation, and the number or volume concentration of the mode.

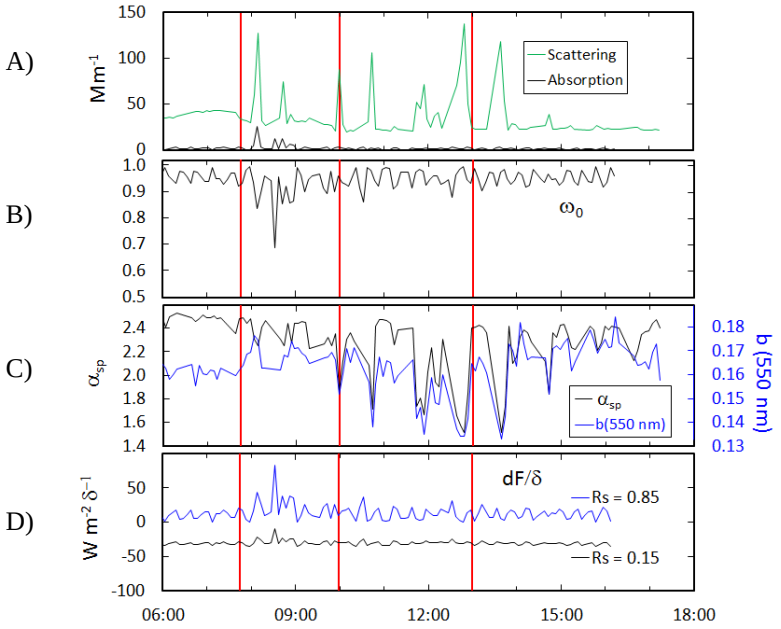

Fig. 8. Optical properties of aerosol observed in the aerosol cottage. **(A)** scattering and absorption coefficients at λ = 550 nm, **(B)**: single-scattering albedo at λ = 550 nm, **(C)** Ångström exponent of scattering over 450–700 nm (α_{sp}) and backscatter fraction (b) at λ = 550 nm; **(D)** intrinsic aerosol forcing efficiency for two surface reflectances (R_s).

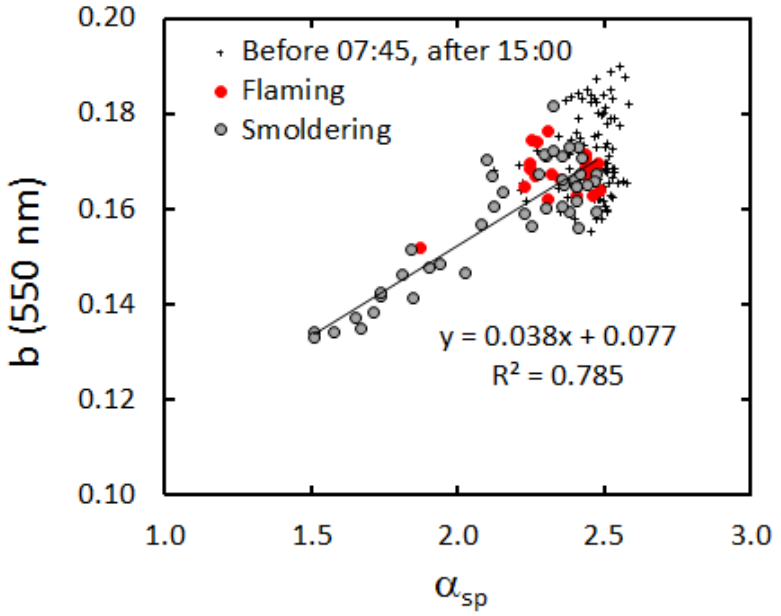

Fig. 9. Backscatter fraction (b) at λ = 550 nm vs. Ångström exponent of scattering (α_{sp}) in the aerosol cottage before the flaming phase and after the last plume was observed (crosses), during the flaming phase (red circles), and during the smoldering phase (grey circles). The regression line was fitted with the smoldering-phase data.

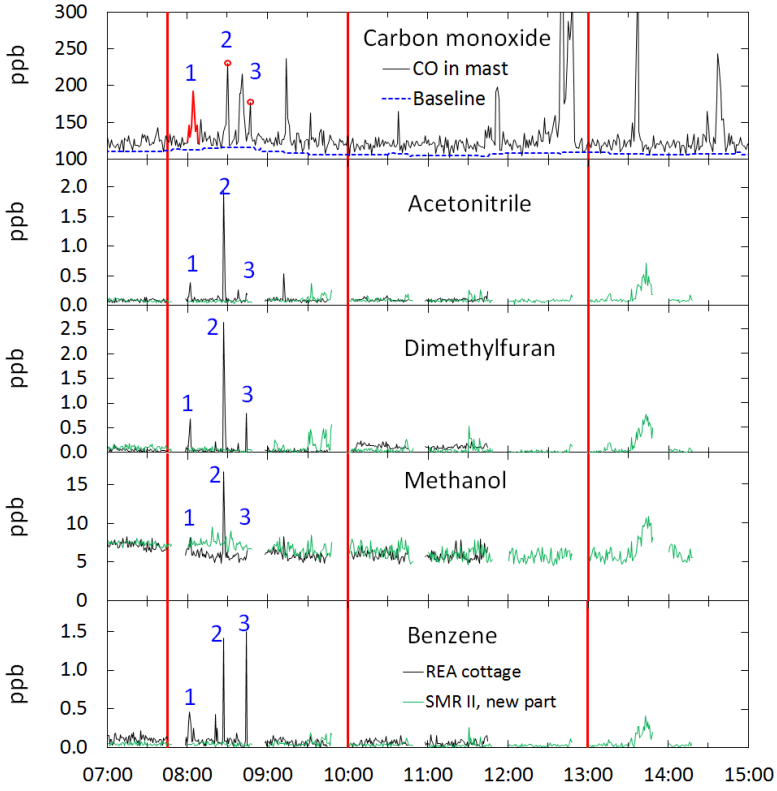

Fig. 10. Data of selected VOCs measured with PTR-MS and carbon monoxide measured in the mast at all altitudes. The numbers on the peaks and the red line for CO in peak 1 denote the data that that were used for the regressions in Fig. 10 and Table 3.

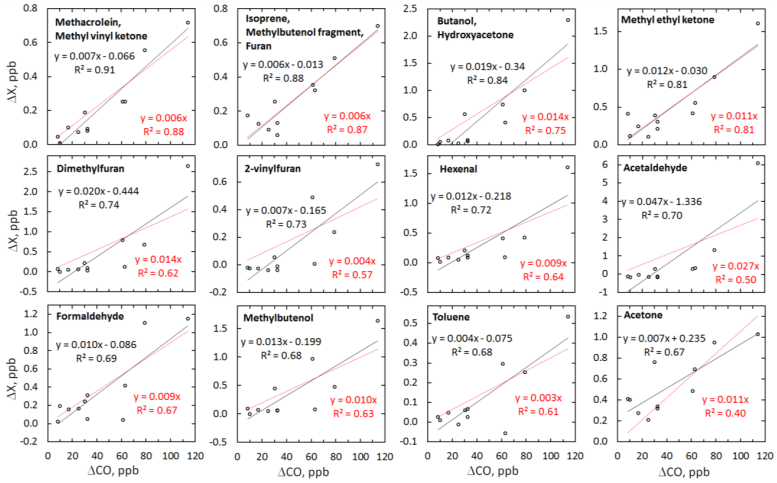

Fig. 11. Relationships of excess concentrations (ΔX) of organic trace gases to excess carbon monoxide (ΔCO) concentrations in the smoke plume peaks presented in Fig. 9. The black lines and formulas denote linear regressions without forcing the offset to zero and the red lines and formulas linear regressions with forcing the offset to zero.

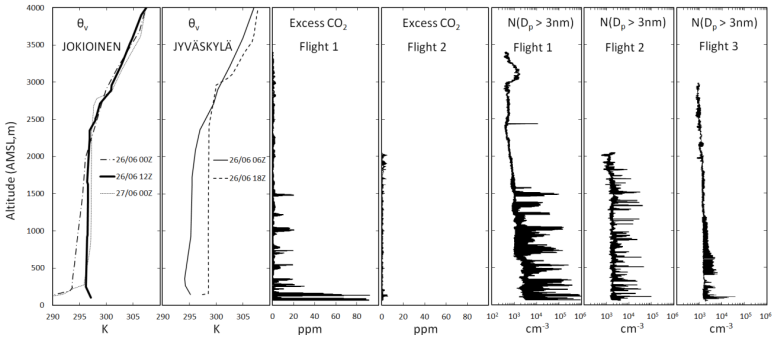

Fig. 12. Vertical profiles of virtual potential temperature (θ_v), excess CO_2 and particle number concentrations during the experiment day. For flight 3 no excess CO_2 data are shown because they did not deviate from zero. The θ_v data are from meteorological soundings from two sites, the Jokioinen observatory and the Tikkakoski airport in Jyväskylä.

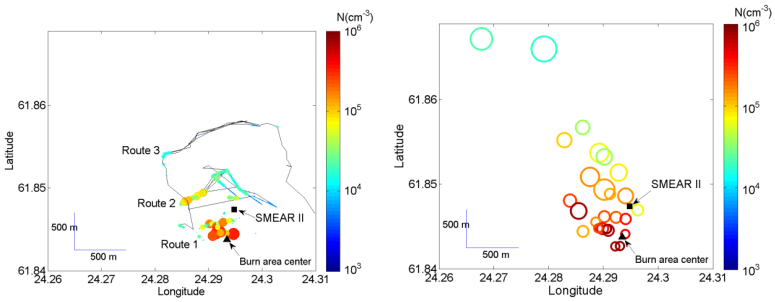

Fig. 13. Horizontal spread of the smoke plume **(A)** at the ground level as observed with the portable CPCs and **(B)** as observed in the aircraft. In **(A)** both the diameter and the symbol size are scaled according to the concentration. In **(B)** the colour scale is for the concentration and the circle size is scaled according to the diameter of the plume.

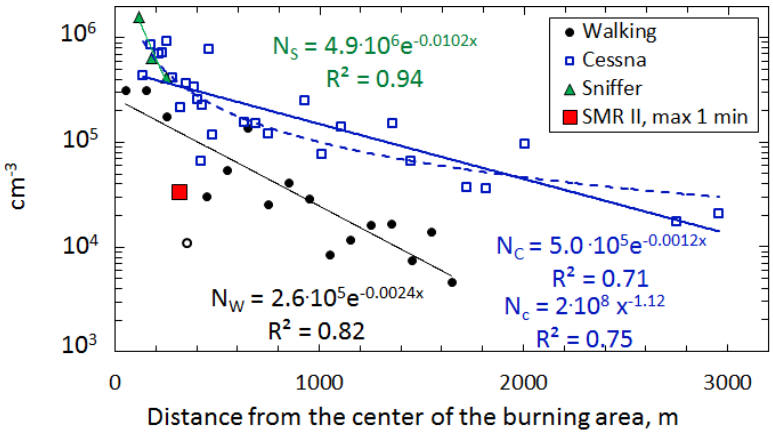

Fig. 14. Particle number concentration as a function of 3-dimensional distance from the center of the burning area measured in the Cessna, with the portable CPCs on ground (walking, N_W), in the aeroplane (Cessna, N_C), and on ground in the van (*Sniffer*, N_S). The walking data points are the maximum concentrations of each 100 m distance bin, the aircraft data points are the maxima in each plume passage and the *Sniffer* data points the 3–5 min average concentrations measured at three standing locations of the van. The SMR II data point denotes the maximum 1 min particle number concentration in the aerosol cottage during the experiment. The solid lines denote fittings of the exponential function $N_0 e^{-kx}$ and the dashed line the fitting of a power law $N_0 x^{-b}$ and where x is the distance from the center of the burn area.